minerals

MDPI

Article

Geochemistry and Zircon U-Pb-Hf Isotopes of Metamorphic Rocks from the Kaiyuan and Hulan Tectonic Mélanges, NE China: Implications for the Tectonic Evolution of the Paleo-Asian and Mudanjiang Oceans

Zuozhen Han [1,2], Jingjing Li [1], Zhigang Song [1,*], Guyao Liu [3], Wenjian Zhong [1], Lihua Gao [1] and Qingxiang Du [1]

[1] College of Earth Science and Engineering, Key Laboratory of Depositional Mineralization & Sedimentary Mineral of Shandong Province, Shandong University of Science and Technology, Qingdao 266590, China; hanzuozhen65@126.com (Z.H.); skdmyb@163.com (J.L.); zwjlangya@126.com (W.Z.); glhxx@163.com (L.G.); geodqx@foxmail.com (Q.D.)

[2] Laboratory for Marine Mineral Resources, Qingdao National Laboratory for Marine Science and Technology, Qingdao 266071, China

[3] Tongling Nonferrous Shares Tianmashan Gold Mining Co., Ltd., Tongling 244000, China; guyaoliu89@163.com

* Correspondence: zgsong@sdust.edu.cn

Received: 4 September 2020; Accepted: 20 September 2020; Published: 22 September 2020

Abstract: The Late Paleozoic–Early Mesozoic tectonic evolution of the Changchun-Yanji suture (CYS) was mainly associated with the Paleo-Asian and Mudanjiang tectonic regimes. However, the spatial and temporal overprinting and variations of these two regimes remains are still dispute. In order to evaluate this issue, in this contribution, we present new zircon U-Pb ages and a whole-rock geochemical and zircon Hf isotopic dataset on a suite of metamorphic rocks, including gneisses, actinolite schist, leptynites, and biotite schists, from tectonic mélanges in northern Liaoning and central Jilin provinces, NE China. Based on zircon LA-ICP-MS U-Pb dating results, protoliths show wide ranges of aging spectrum, including Paleoproterozoic (2441 Ma), Early Permian (281 Ma), Late Permian (254 Ma), and Late Triassic (230 Ma). The Permian protoliths of leptynites from the Hulan Tectonic Mélange (HLTM) and gneisses from the Kaiyuan Tectonic Mélange (KYTM) exhibit arc-related geochemical signatures, implying that the Paleo-Asian Ocean (PAO) did not close prior to the Late Permian. The Late Triassic protoliths of gneisses from the KYTM, in combination with previously reported coeval igneous rocks along the CYS, comprises a typical bimodal igneous suite in an E–W-trending belt, suggesting a post-orogenic extensional environment. Consequently, we infer that the final closure of the PAO took place during the Early–Middle Triassic. The Early Permian protoliths of biotite schists from the HLTM are alkali basaltic rocks and contain multiple older inherited zircons, which, in conjunction with the geochemical features of the rocks, indicate that they were generated in a continental rift related to the initial opening of the Mudanjiang Ocean (MO). Data from this contribution and previous studies lead us to conclude that the MO probably opened during the Middle Triassic, due to the north–south trending compression caused by the final closure of the PAO.

Keywords: tectonic mélange; metamorphic rocks; zircon U-Pb geochronology; geochemistry; Paleo-Asian Ocean; Mudanjiang Ocean

1. Introduction

Mélanges are defined as mixed rock bodies and exotic blocks yielding different ages, origins, and/or dissimilar metamorphic grades, and the stratigraphic continuity has been completely disrupted at a scale of meters to tens of meters [1–3]. They play a key role in the interpretation of sutured ocean basins, including those that have experienced metamorphism and deformation during continental collision [4–7]. A case in point is the tectonic evolution of the NE China, which has traditionally been considered to be the eastern segment of the Central Asian Orogenic Belt (CAOB; Figure 1a) [8–21]. During its long tectonic evolutionary history, the NE China witnessed the amalgamation of several micro-continental blocks (Figure 1b) and the final closure of the Paleo-Asian Ocean (PAO) during the Paleozoic to Early Mesozoic, which was subsequently overprinted by post-Mesozoic Mongol-Okhotsk and circum-Pacific tectonic regimes [22–26]. Therefore, the NE China is a key area to understand the NE Asian tectonic evolution and its regime transition from the Paleozoic to Mesozoic.

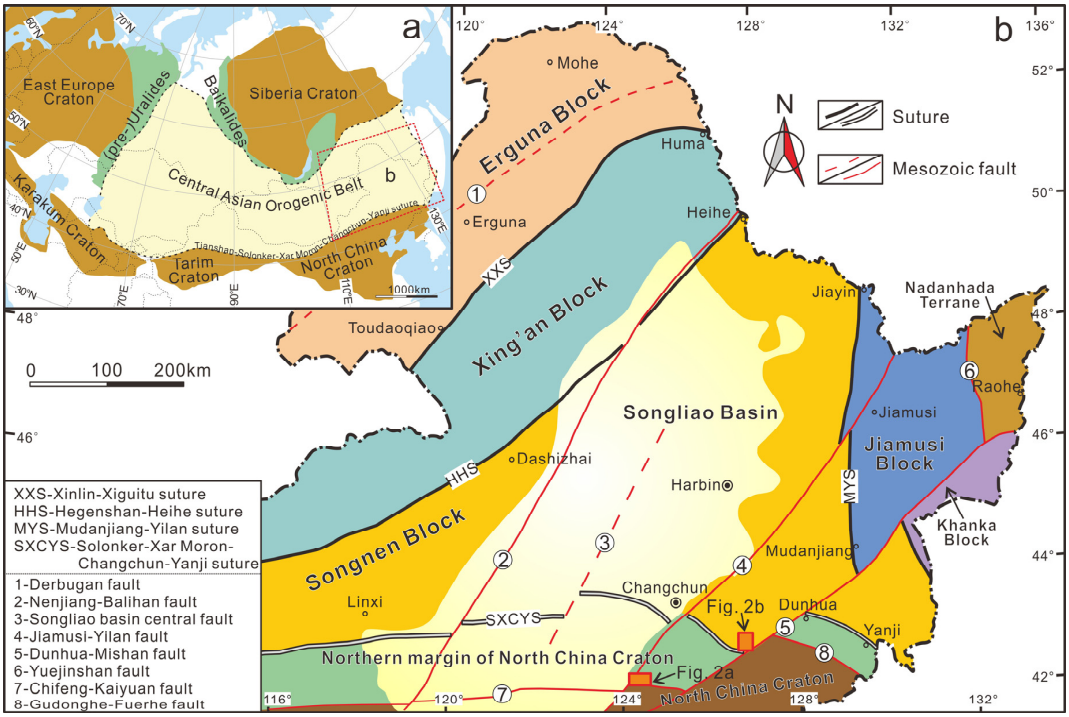

Figure 1. (**a**) Tectonic outline of the Central Asian Orogenic Belt (CAOB) and surrounding regions (modified from the work in [27]); (**b**) Tectonic sketch map of NE China (modified from the work in [11]).

Located between the combined NE China blocks and the North China Craton (NCC), the Changchun-Yanji suture (CYS) is traditionally regarded as the locus of the final closure of the PAO [9–11,28–30]. Many studies have attempted to delineate the architecture of the suture zone and to reconstruct its evolutionary history; however, there is much left to debate on its spatial distribution, temporal evolution, and eventual suturing. While estimates of timing vary from pre-Late Devonian [31–33] through the Early–Middle Permian [34] to the Late Permian–Middle Triassic or even later [35–54], there continues to be ambiguity as to whether subduction occurred via a bidirectional [40–42,44–46] or single-sided southward [36,37] subduction geometry. Furthermore, increasing evidence indicates that the Mudanjiang Ocean (MO), which was between the Songnen and Jiamusi blocks, participated in the tectonic evolution of NE China during the Late Permian to Mesozoic [55–68]. Therefore, some researchers recently proposed that the CYS is the southern margin of the Jilin–Heilongjiang high-pressure metamorphic belt which is closely related to the closure of the MO, rather than the eastward extension of the Solonker-Xar Moron-Changchun suture (SXCS) [69–72].

Obviously, the above controversies are mainly attributed to fuzzy discrimination of the above two tectonic systems, that is, the PAO and the MO. Therefore, further work on the tectonic evolution of the CYS is vital to understanding the tectonics of NE China. Fortunately, various Paleozoic–Mesozoic fragments [14,21,28,38,40,41,48], which provide important keys to understanding the tectonic evolution of suture zone, were preserved within tectonic mélanges along the CYS during orogeny. In this contribution, whole-rock geochemical and zircon U-Pb and Lu-Hf isotope data for metamorphic rocks that include in tectonic mélanges from northern Liaoning and central Jilin provinces are presented. These data are used to constrain the formation age, lithology, and origin of the different protoliths, and to place constraints on the Permo–Triassic tectonic evolution of the CYS.

2. Geological Context and Previous Work

The Kaiyuan and Hulan areas are located in northern Liaoning and central Jilin provinces, along the eastern segment of the northern margin of the NCC and the southeastern margin of the CAOB (Figure 1b). It is adjacent to the Songliao Basin and the Dunhua-Mishan Fault to the west and east, respectively (Figure 1b). This region is dominated by the voluminous occurrence of Phanerozoic granitoids, which can be mainly divided into three phases: (1) Early–Middle Paleozoic [73], (2) Permian–Triassic [36,40,42,43,45,46,74,75], and (3) Jurassic [26,76]. There are also limited and scattered outcrops of subduction-accretionary complexes dispersed in these granitoids. Despite recent studies have suggested that these various complexes are made up of mixed blocks with different ages and origins, accretionary complexes, and Paleozoic–early Mesozoic intrusive rocks and tectonic slices [14,21,28,38,40,41,48].

The Kaiyuan tectonic mélange (KYTM) is a suite of amphibolite-greenschist facies meta-volcanic and meta-sedimentary rocks that crop out ~10 km to the northeast of Kaiyuan (Figure 2a). It consists of meta-andesite, meta-basalt, leptynite, gneiss, schist, and marble [38,41,48]. The KYTM has discontinuous and poor exposures, and it underwent severe later-stage deformation and weathering. As a consequence, different viewpoints have been proposed to classify the components of the KYTM. In addition, different names have been given to the KYTM by previous studies, such as Kaiyuan Group, Qinghezhen Group, and Liaohe Group [77–79]. The KYTM was once regarded as Proterozoic supracrustal strata, however a series of tectonic blocks/slices with different ages and origins have been identified during some recent investigations [38,41,48,80].

The Hulan tectonic mélange (HLTM) consists of a series of metamorphic volcanic and sedimentary rocks poorly exposed in the Hongqiling–Hulan area, central Jilin Province (Figure 2b). It was initially named as the Hulan Group and was subdivided, from bottom to top, into the Huangyingtun, Xiaosan'gedingzi, and Beichatun formations [81,82]. The Beichatun Formation is dominated by marble, crystalline limestone, and slate. The presence of *Thamnopora* sp., *Cladopora* sp., *Fenestella* sp., and *Polypora* sp. in Beichatun limestones, coupled with regional geological outline, show a late Silurian age [81]. The Xiaosan'gedingzi Foramtion is composed of marble, quartzite, schist, leptite, and biotite leptynite, whereas the Huangyingtun Formation is dominated by marble, leptynite, and gneiss [81]. Some early studies proposed that the Hulan tectonic mélange formed during the Cambrian–Ordovician [81], the Ordovician [83], the Cambrian–Silurian [84], or the Cambrian–Devonian [82]. Wu et al. [28] reported a maximum age of deposition of 287 ± 6 Ma and considered that the Hulan tectonic mélange is not a true stratigraphic sequence based on the detrital zircon U-Pb ages from a meta-sedimentary rock and fossil evidences.

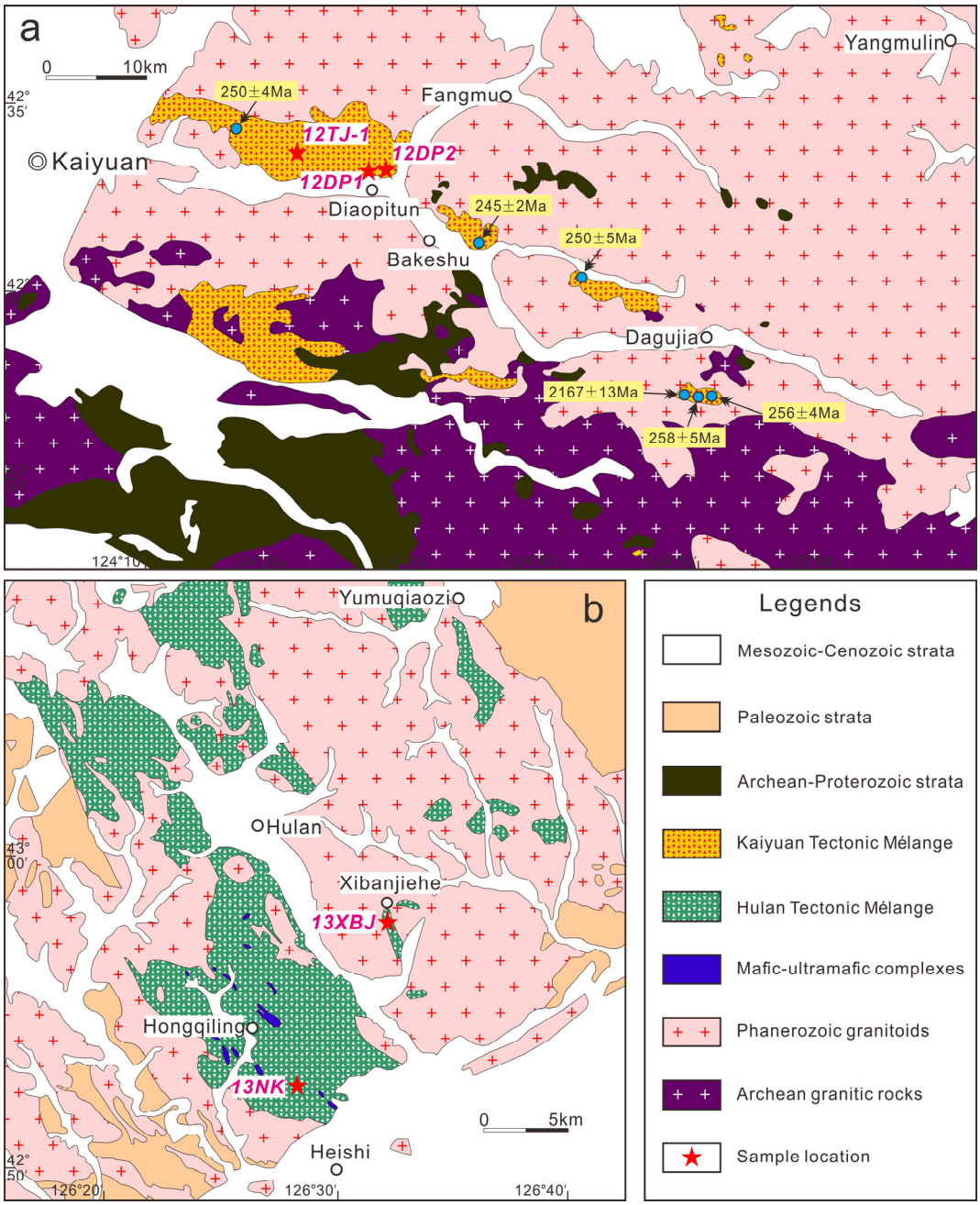

Figure 2. Geological map of (**a**) Kaiyuan and (**b**) Hulan regions showing the distribution of Kaiyuan and Hulan tectonic mélanges (modified from the works in [28,41], respectively). Age data are referred from the works in [38,41,48,79].

3. Sampling and Petrography

We collected ten gneisses (12DP1-1~5, 12DP2-1~5) and one schist (12TJ-1) from the KYTM, and eight leptynites (13NK-1~8) and five schists (13XBJ-1~5) from the HLTM (Figure 2). The lithologies, locations, textures, structures, and mineralogical composition of the studied samples are summarized in Table 1, and their petrographic features are shown in Figure 3.

Table 1. Summary of the sample locality, lithology, mineral assemblages, and protoliths ages.

Sample	GPS Location	Lithology	Mineral Assemblages	Protoliths [1]	Ages (Ma) [2]
12DP1	N 42°31′17″ E 124°26′06″	Hornblende epidote plagioclase gneiss	Qz (2–3 vol.%), Afs + Pl (47–52 vol.%), Ep (25–30 vol.%), Hbl (10–15 vol.%), Ttn, Ap, Zrn, Opq	Basalt	230
12DP2	N 42°31′17″ E 124°26′09″	Hornblende biotite plagioclase gneiss	Qz (1–2% vol.), Pl (63–69% vol.), Bt (20–27% vol.), Hbl (3–5 vol.%), Ttn, Ap, Zrn, Opq	Basalt	254
12TJ-1	N 42°33′04″ E 124°21′03″	Actinolite schist	Qz + Pl (55–60 vol.%), Act (30–37 vol.%), Bt (3–5 vol.%)	Intermediate rock	2441
13NK	N 42°51′59″ E 126°28′11″	Biotite hornblende leptynite	Qz (15–17 vol.%), Pl (50–55 vol.%), Hbl (20–23 vol.%), Bt (5 vol.%), Opq	Dacite	281
13XBJ	N 42°58′17″ E 126°31′57″	Hornblende biotite schist	Qz + Pl (10–15 vol.%), Bt (80–85 vol.%), Hbl (5 vol.%)	Basalt	281

[1] The protoliths of the metamorphic rocks were based on a comprehensive analysis of field observation, mineral assemblage, and geochemistry. [2] Measured zircon U-Pb ages in this study.

The 12DP1 and 12DP2 are grayish green gneisses collected from the Zhaobeishan Formation of the KYTM near the Diaopitun village (Figure 2a). 12DP1 (Figure 3a) is a hornblende-epidote-plagioclase gneiss with a granoblastic texture (Figure 3b). This rock is mainly composed of plagioclase (45–50 vol.%), epidote (25–30 vol.%), hornblende (10–15 vol.%), quartz (2–3 vol.%), and alkali feldspar (1–2 vol.%). Minor titanite, apatite, zircon, and opaque minerals form the accesory minerals suites. Plagioclase and epidote grains vary in size (0.1–2.5 mm) and display irregular margins. Hornblende occurs around or between grains of plagioclase and epidote and weakly defines the foliation of the rock. 12DP2 (Figure 3c), a hornblende-biotite-plagioclase gneiss, has a lepidogranoblastic texture (Figure 3d). It is made up of plagioclase (63–68 vol.%); biotite (20–25 vol.%); hornblende (3–5 vol.%); quartz (1–2 vol.%); and accessory titanite, apatite, zircon, epidote, and opaque minerals. Plagioclase crystals display irregular and crenulated margins and partially altered to sericite. Biotite and horblende commonly develops surrounding plagioclase and are orientated along the foliation. The secondary carbonatization (mainly occurred within veins), chloritization, and uralitization of mafic minerals can be observed in the above samples.

Sample 12TJ-1 is a grayish green actinolite schist (Figure 3e,f), sampled collected from the Tongjiatun Formation near the Tongjiatun village. Microscopically, the rock presents a weak schistose structure and microscopic fibrogranoblastic texture and made up of microscopic felsic (Pl + Qz) minerals (55–60 vol.%), acicular actinolite (30–35 vol.%), and biotite (3–5 vol.%). The weakly orientated actinolite and biotite define the planar foliation of the rock. In addition, the rock is cross-cut by some quartz veins in some portions.

13XBJ-1 a chlorite-hornblende-biotite schist sampled from the Xiaosan'gedingzi Formation (Figure 2b), is grayish-green in color, contains schistose, and has a lepidogranoblastic texture (Figure 3g–i). The main minerals are biotite (70–75 vol.%), hornblende (5 vol.%), quartz (10–15 vol.%), and plagioclase (2–3 vol.%). Chlorite is unevenly distributed.

13NK-1 a biotite-hornblende leptynite sampled from Huangyingtun Formation (Figure 2b), is khaki in color, and has a massive structure and granoblastic texture (Figure 3j–l). It is mainly made up of plagioclase (60–65 vol.%), hornblende (15–20 vol.%), quartz (5–10 vol.%), and biotite (5–10 vol.%). Apatite, zircon, and opaque minerals form the accessory mineral suite.

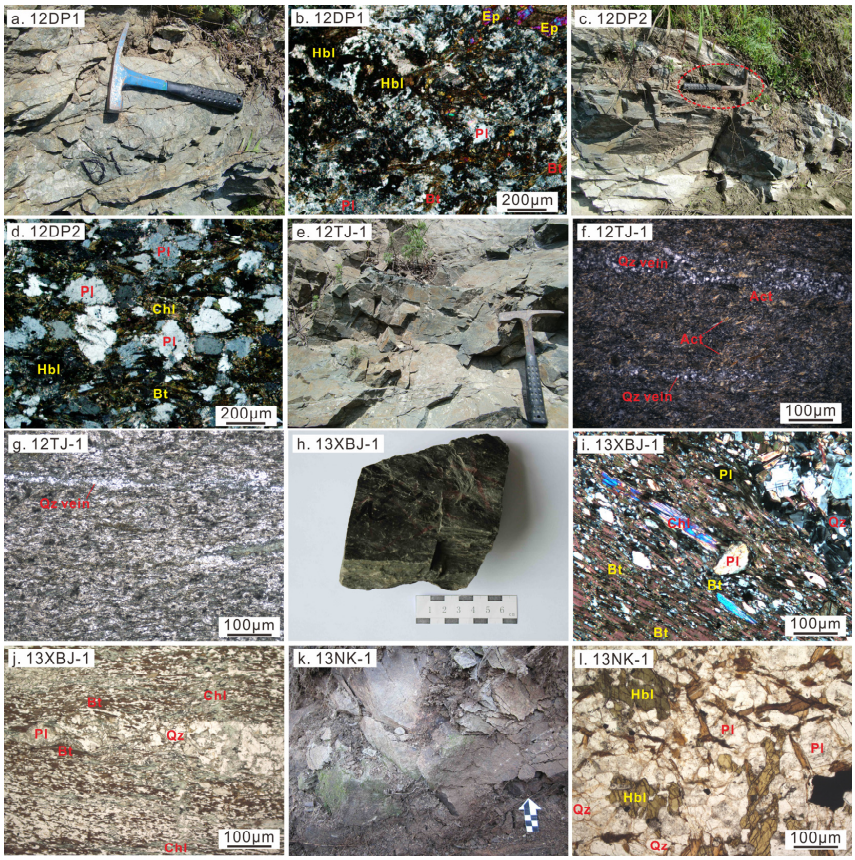

Figure 3. Field photographs and photomicrographs showing representative metamorphic rocks from the KYTM and HLTM. (**a**,**b**) Hornblende-epidote-plagioclase gneiss; (**c**,**d**) hornblende-biotite-plagioclase gneiss; (**e**–**g**) actinolite schist; (**h**–**j**) chlorite-hornblende-biotite schist; (**k**,**l**) biotite-hornblende leptynite. Mineral abbreviations according to the work in [85]. Plagioclase (Pl), quartz (Qz), biotite (Bt), hornblende (Hbl), actinolite (Act), epidote (Ep), chlorite (Chl).

4. Analytical Techniques

4.1. Zircon U–Pb Age and Trace Element Data

Zircons were separated using a Frantz magnetic separator and heavy liquids (bromoform, 2.89 g/cm^3; diiodomethane, 3.32 g/cm^3) at the Hebei Regional Geological Survey, China. Cathodoluminescence (CL) images were obtained using JEOL JXA-8900RL scanning electron microscope at the State Key Laboratory of Continental Dynamics, Northwest University, Xi'an, China.

Zircon trace elements and U-Th-Pb isotopes were simultaneously determined using an Agilent 7500a ICP-MS equipped with a 193 nm laser ablation system GeoLas 2005 at the State Key Laboratory of Continental Dynamics, Northwest University, Xi'an, China. The instrument parameter and detail procedures were described by Yuan et al. (2004) [86]. The laser spot size was 32 μm with a repetition rate of 6 Hz during the analyses. The zircon 91500 was used as an external standard for age calibration, and the NIST SRM 610 silicate glass was applied for instrument optimization. The laser spot size was 32 μm during the analyses. Isotopic ratios and element contents were calculated by using the GLITTER 4.0 [87]. The age calculation and Concordia plots were made using Isoplot (Ver. 3.0) [88]. Concordance was calculated as (^{206}Pb/^{238}U/^{207}Pb/^{235}U) × 100 with concordance defined between 90% and 110%.

4.2. Whole-Rock Major and Trace Element Analyses

The major and trace element concentrations of the whole-rock samples were determined at the Supervision and Inspection Center of Mineral Resources, the Ministry of Land and Resources of Jinan,

China. The concentrations of SiO_2 and Al_2O_3 were analyzed using the gelatin coagulation gravimetic method and the xylenol orange method, respectively. The other major oxides and some trace elements, (Ba, Sr, V, and Cr) were determined by IRIS-Intrepid ICP atomic emission spectrometer (AES) using the standard analytical protocol of GB/T14506-2010 for the oxides. Detailed analytical procedures are similar to those described by Rudnick et al. (2004) [89]. Analytical uncertainties range from 1% to 5%. The other trace element concentrations were determined using an X-Series 2 ICP-MS, and the analytical procedures are similar to those described by Li (1997) [90]. An internal standard solution containing the single element Rh was used to monitor signal drift during counting. The analytical precision for major elements is better than 1% and for trace elements is generally better than 5%.

4.3. In situ Zircon Lu-Hf Isotopic Analyses

Zircon Hf isotope analyses were conducted using a Nu Plasma HR MC-ICP-MS that was coupled with a Geolas 2500 laser-ablation system at the State Key Laboratory of Continental Dynamics, Northwest University, Xi'an, China, using techniques and analytical procedures described by Xu et al. (2004) [91]. A laser spot size of 44 μm and a repetition rate of 10 Hz were used. Ratios used for the corrections were 0.5886 for $^{176}Yb/^{172}Yb$ and 0.02655 for $^{176}Lu/^{175}Lu$ [92]. External corrections were applied to all unknowns, and standard zircons 91500 and GJ were used as external standards and were analyzed twice before and after every 10 analyses. The decay constant for ^{176}Lu of 1.867×10^{-11} year^{-1} [93] and the present-day chondritic ratios of $^{176}Hf/^{177}Hf = 0.282785$ and $^{176}Lu/^{177}Hf = 0.0336$ [94] were adopted to calculate the $\varepsilon_{Hf}(t)$ values. Single-stage model ages (T_{DM1}) were calculated using a depleted mantle with a present-day $^{176}Hf/^{177}Hf$ ratio of 0.28325 and $^{176}Lu/^{177}Hf$ ratio of 0.0384 [95].

5. Results

5.1. Whole-Rock Geochemistry and Protolith Reconstruction

Whole-rock major- and trace-element geochemical data for the Permo–Triassic metamorphic rocks in this study are presented in Table S3. These data are used for classifying the rocks, protolith reconstruction, and determining the tectonic setting of the protoliths.

A preliminary scan of the data allows us to divide the samples into two groups. The Group I (including the 12DP1, 12DP2, 13XB, and 13XBJ) samples show major oxides with SiO_2 ranging from 43.87 to 51.05 wt% and total alkalis ($K_2O + Na_2O$) ranging from 1.02 to 4.35 wt%, defining a mafic composition with some enrichment of alkaline elements. In contrast, the Group II (the 13NK) samples have SiO_2 ranging from 63.22 to 68.92 wt% and total alkalis ranging from 6.00 to 6.91 wt%, defining a felsic composition. The $Al_2O_3/(Al_2O_3 + CaO + Na_2O + K_2O)$ ratio of all samples is less than 0.65, indicating that the metamorphic rocks may be orthometamorphites [96]. In the Zr/Ti versus Ni diagram (Figure 4a) for discrimination between igneous and sedimentary amphibolite protoliths [97], the Group I samples plot in the igneous field, indicating igneous protoliths for these samples. The DF3 and DF4 discriminant functions were proposed by Shaw (1972) [98] to distinguish between silicic volcanic and clastic gneiss protoliths. The positive DF3 (2.08–4.02) and DF4 (0.11–1.75) values of the 13NK samples suggest that their protoliths might be silicic volcanic rocks.

As all samples have been metamorphosed and Na_2O and K_2O tend to be mobile during the process of metamorphism and alteration, we use the Zr/TiO_2 versus Nb/Y diagram instead of the total alkalis versus SiO_2 diagram for further discrimination (Figure 4b). In this diagram, the studied metamorphic rocks fall in different compositional groups, with basaltic samples in the basalt/subalkaline basalt and alkali basalt fields, and felsic samples in the rhyodacit/dacite field (Figure 4b).

With regard to trace elements, all the samples are characterized by varying light rare earth element (LREE)-enriched patterns in chondrite-normalized rare earth element (REE) diagram (Figure 5a–c), with $(La/Yb)_N$ values of 2.76–20.20 and negligible/negative Eu anomalies of 0.46–0.99. The 12DP2 samples have marked higher contents of total REEs (338.62–487.96 ppm) and stronger LREE enrichment

than the other samples. In the primitive mantle-normalized trace element spider diagrams (Figure 5d–f), the 12DP1, 12DP2, and 13NK samples show depletion in high field strength elements (HFSEs) relative to large ion lithophile elements (LILEs), especially in Nb, Ta, P, and Ti. Furthermore, the 12DP1 and 12DP2 samples have notable negative Zr-Hf anomalies (Figure 5d). In contrast, the 13XBJ samples show Oceanic Island Basalt (OIB)-like trace element patterns, without negative Nb-Ta anomalies (Figure 5c,f).

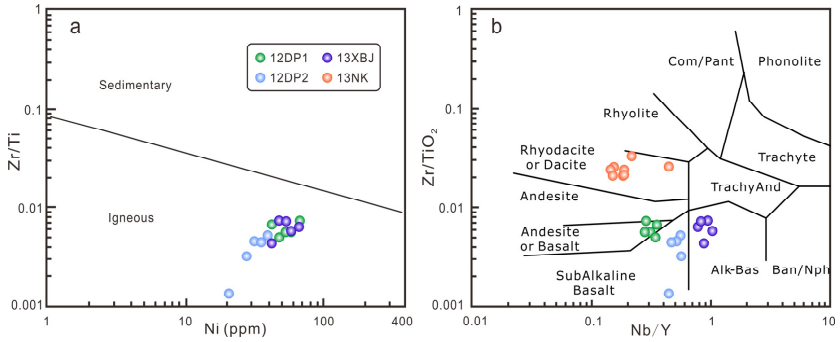

Figure 4. (**a**) Discrimination of volcanic and sedimentary amphibolites, modified after the work in [97]; (**b**) Classification volcanic rocks using relatively inmobile elements, modified after the work in [99].

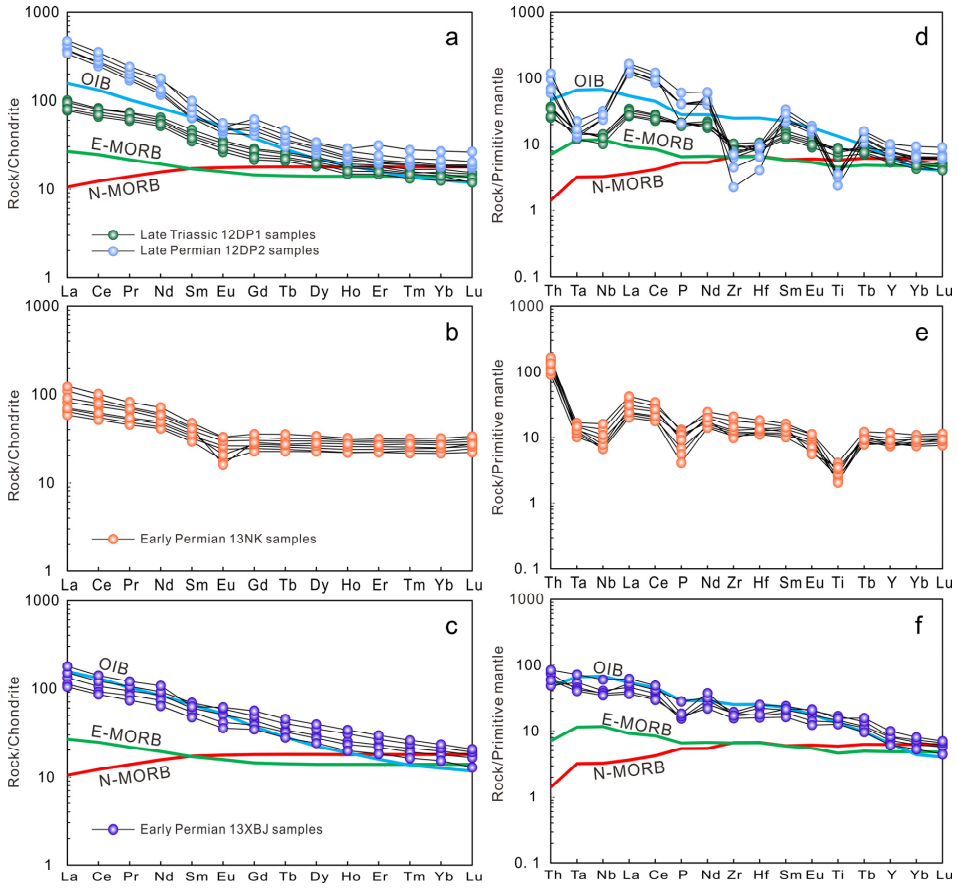

Figure 5. (**a**–**c**) Chondrite-normalized REE patterns and (**d**–**f**) primitive mantle-normalized trace element patterns of PermoTriassic metamorphic rocksin this study. Normalizing values, patterns for N-type mid-ocean ridge basalts (N-MORB), E-type mid-ocean ridge basalts (E-MORB), and oceanic island basalts (OIB) are from [100].

5.2. Zircon Characteristics

Five samples including two gneiss (12DP1-1 and 12DP2-1), two schists (12TJ-1 and 13XBJ-1), and a leptynite (13NK-1) were selected for zircon U-Pb isotopic and rare earth element (REE) analyses. The CL images of analyzed zircons are shown in Figure 6. The analytical results are listed in Tables S1 and S2.

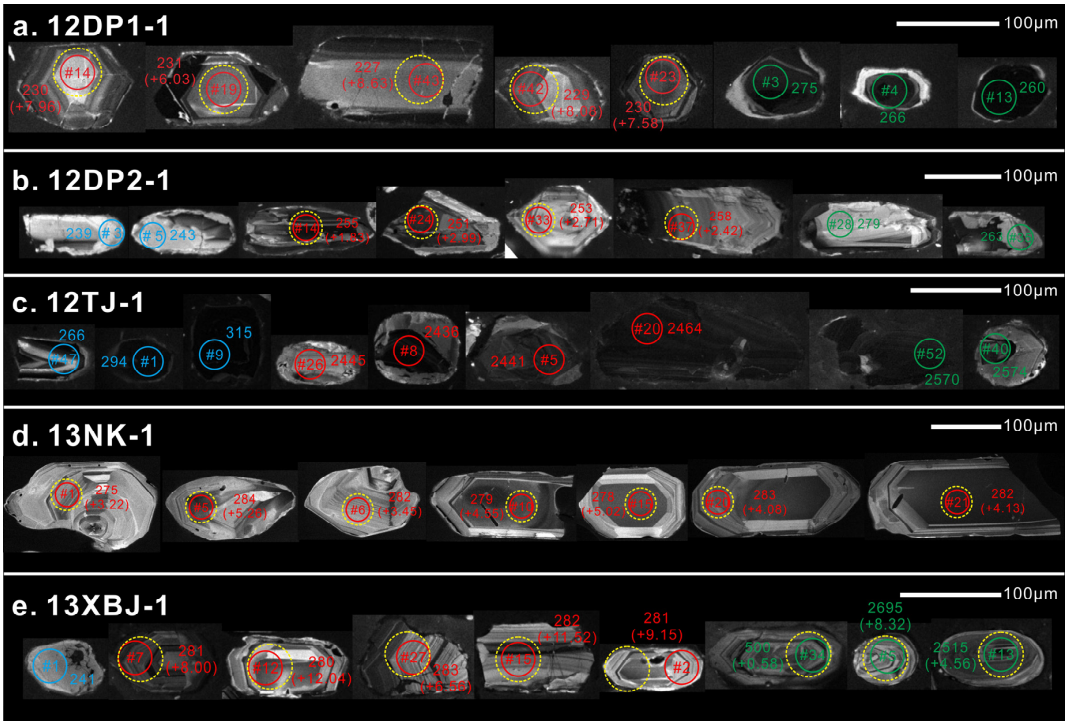

Figure 6. Representative cathodoluminescence (CL) images of zircons from the (**a**,**b**) gneisses, (**c**) actinolite schist, (**d**) leptynite and (**e**) hornblende-biotite schist in this study. The solid-line and dash-line circles represent the locations for U-Pb dating and in situ Lu-Hf isotope analysis, respectively. The numbers show the ages of the zircons (Ma) and the $\varepsilon_{Hf}(t)$ values.

5.2.1. Zircon Morphology

Zircon grains from sample 12DP1-1 are translucent to transparent, equant to long prismatic, sub-rounded, with some occurring as fragments. Most zircons are pink; a few are roseal. They have grain sizes of 70 to 190 μm, with ratios of length to width ranging from 1:1 to 3:1. Grains are euhedral and subhedral with multifactor characteristics. In CL images, most of the zircons show broad growth zoning (Figure 6a), which is typical feature of zircons from magmatic rocks with relatively low silica content [101], while a small amount of zircons are dark in color, showing no clear growth zoning (e.g., # 3, # 4, and # 13; Figure 6a). In addition, rare zircons (e.g., # 3, # 4, and # 13) show thin rims with strong CL brightness (Figure 6a), which are interpreted as metamorphic overgrowth, however, they are too thin to be analyzed.

Zircons from sample 12DP2-1 are yellowish pink, translucent to transparent, and subhedral, and show oval (e.g., # 5) to long prismatic shape. Crystal lengths are approximately 50 to 300 μm, with aspect ratios of 1:1 to 3.5:1. There are mainly two types of zircon with complex internal structures as revealed by CL imaging (Figure 6b): (1) some zircons show oscillatory, blurred oscillatory or planar zoning without core-rim structure, which are interpreted as magmatic origin but suffered low degrees of metamorphic recrystallization (e.g., # 5); (2) the others exhibit core-rim structure and core-rim boundaries are generally irregular. The cores are characterized by oscillatory, cloudy, weak zoned, or unzoned structures, indicating that they are magmatic origin but reworked by varying degrees of recrystallization. Most of the rims cut the primary zones of cores, indicating of metamorphic

recrystallization. Rare rims and cores have regular boundaries (e.g., # 24), which are interpreted to be metamorphic growth.

Zircons in sample 12TJ-1 are roseal, transparent, and subheral to anhedral. Most of them are oval to round, whereas some grains show prismatic shape. The lengths of these zircons range from 50 to 230 μm, with aspect ratios of 1:1 to 2.5:1. As revealed by the CL images (Figure 6c), both the recrystallization of protolith zircon and the growth of metamorphic zircon occur in this sample. Some zircons are unzoned or weakly zoned with strong or weak luminance (e.g., # 1 and # 9). The others show core-rim structures, which always occur as complicated cores surrounded by wide rims. Only a few of the cores show clear oscillatory zoning (e.g., # 8 and # 11). Most of the cores are unzoned or have cloudy zoning. The rims have strong CL luminescence and unzoned textures.

The majority of zircons from sample 13NK-1 are yellowish pink, transparent, euhedral to subhedral, and prismatic. Rare grains are sub-rounded. They have grain sizes of 40 to 400 μm, with ratios of length to width ranging from 1:1 to 3.5:1. CL imaging revealed that these zircons show clear oscillatory and sector zoning (Figure 6d). Zircons from sample 13XBJ-1 are yellowish pink, transparent and euhedral to subhedral. Most of them are prismatic, and a few crystals are sub-rounded in shape. Lengths of these grains range from 50 to 200 μm, with aspect ratios of 1:1 to 2:1. As shown in CL images (Figure 6e), most of them show clear oscillatory zoning, and a few grains are unzoned or have cloudy zoning, with relatively low CL brightness.

5.2.2. Zircon U-Pb Ages

For sample 12DP1-1, a hornblende-epidote-plagioclase gneiss from the KYTM, sixty-three age measurements were made in 63 zircon grains and 50 concordant ages were obtained (Table S1, Figure 7a). The well-zoned zircons contain Th and U contents of 34 to 604 ppm and 83 to 755 ppm, respectively, yielding relatively high Th/U ratios of 0.20 to 1.45, and 41 grains yield concordant $^{206}Pb/^{238}U$ ages of 233 to 227 Ma with a weighted mean of 230 ± 1 Ma (MSWD = 0.14), while spots # 12 and # 34 give older concordant $^{206}Pb/^{238}U$ ages of 372 and 355 Ma, respectively (Figure 7a). The unzoned or weak zoned zircons show relatively low Th contents of 29 to 59 ppm but high U contents of 414 to 1057 ppm to yield Th/U ratios of 0.05 to 0.08, which is typical for metamorphically grown zircon [102–105]. The seven spots on these zircons are concordant, with apparent $^{206}Pb/^{238}U$ ages of 253 to 275 Ma (Figure 7a).

For sample 12DP2-1, a hornblende-biotite-plagioclase gneiss from the KYTM, forty-two age measurements were made in different zircon domains of 42 grains and 34 concordant ages were obtained (Table S1, Figure 7b). All the analyses obtained from different domains yield variable Th and U contents of 13 to 1749 ppm and 51 to 1837 ppm, respectively, with high Th/U ratios of 0.26 to 1.75. Seven spots on rims are concordant or nearly concordant, with apparent $^{206}Pb/^{238}U$ ages of 246 to 236 Ma and a weighted mean of 242 ± 4 Ma (MSWD = 0.51), which is interpreted to date Triassic-aged metamorphism in the Kaiyuan area. Twenty-seven analyses on cores and zircon grains without core-rim structure give older $^{206}Pb/^{238}U$ ages ranging from 328 to 250 Ma.

For sample 12TJ-1, a actinolite schist from the KYTM, fifty-four analyses were obtained from different zircon domains of 53 grains, yielding a wide range of $^{206}Pb/^{238}U$ ages from 2974 to 264 Ma (Table S1; Figure 7c,d). More than 70 percent (39 of 54) of analyses on different domains show $^{207}Pb/^{206}Pb$ ages of ~2.5 Ga and variable Th and U contents of 11 to 453 ppm and 53 to 1271 ppm, respectively, with Th/U ratios of 0.15 to 1.98. The ~2.5 Ga zircons can be divided into two groups: one group defines a discordia line with upper intercept in the concordia at 2570 ± 24 Ma and a lower intercept age at 266 ± 8 Ma (MSWD = 0.74), while the other group defines a discordia line with upper intercept in the concordia at 2441 ± 15 Ma and a lower intercept age at 350 ± 17 Ma (MSWD = 0.069). The $^{207}Pb/^{206}Pb$ weighted mean ages of the two groups are 2572 ± 36 Ma (MSWD = 0.024, n = 8) and 2443 ± 20 Ma (MSWD = 0.038, n = 31), respectively, which are compatible with the upper intercept ages. Therefore, the younger upper intercept age is interpreted to most accurately represent the protolith formation age of the actinolite schist, while the older one is interpreted to represent the crystallization

age of xenocrystic or inherited zircons [106]. The remaining 15 zircons give much younger but scattered $^{206}Pb/^{238}U$ ages between 372 and 264 Ma.

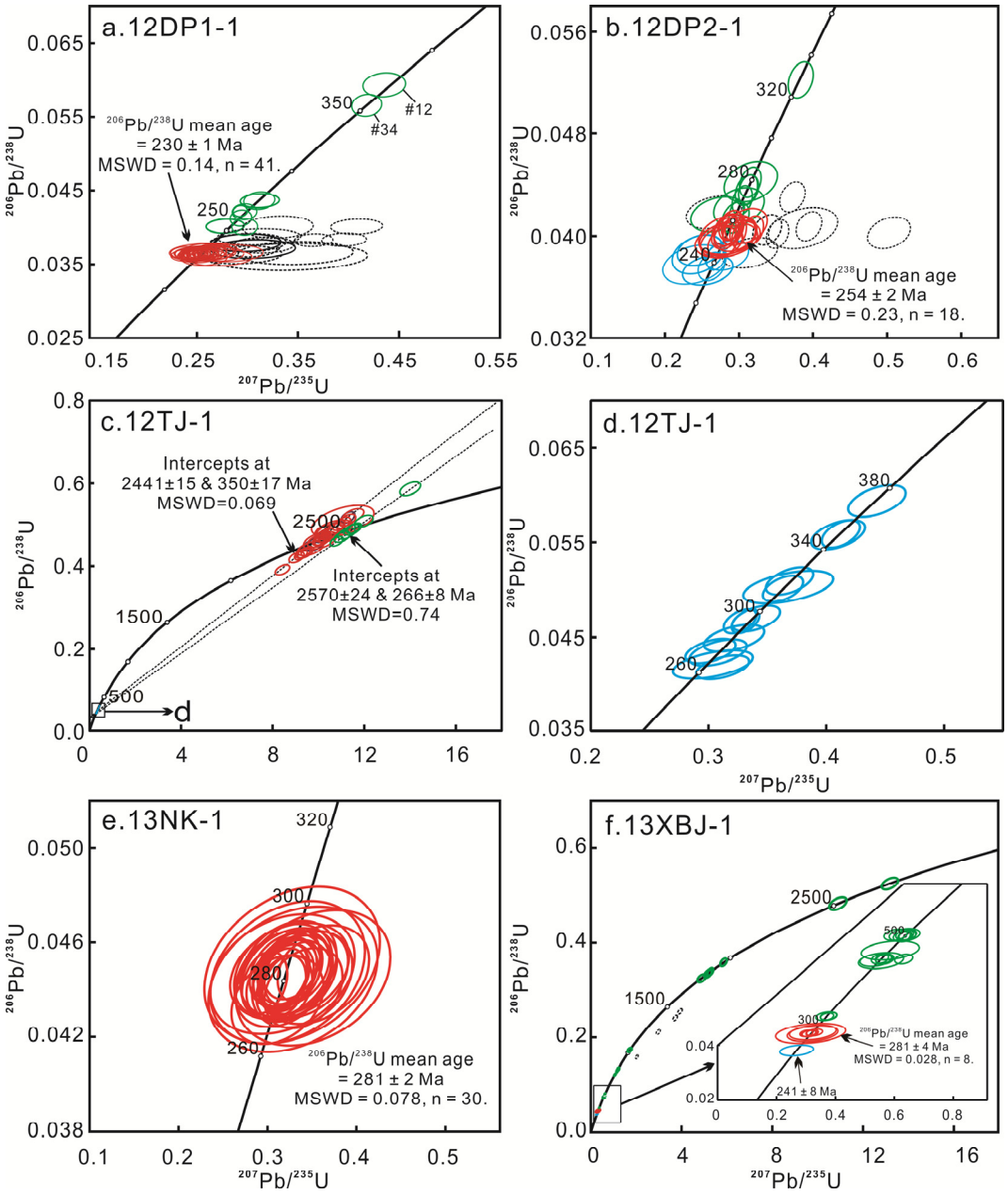

Figure 7. LA-ICP-MS U-Pb concordia diagrams of zircons from the (**a**,**b**) gneisses, (**c**,**d**) actinolite schist, (**e**) leptynite and (**f**) hornblende-biotite schist in this study.

For sample 13NK-1, a biotite-hornblende leptynite from the HLTM, thirty analyses yield concentrated $^{206}Pb/^{238}U$ ages, with a weighted mean age of 281 ± 2 Ma (MSWD = 0.078, n = 30; Figure 7e) for protolith formation. Out of 42 analytical spots, 38 analyses from sample 13XBJ-1 are concordant and have complicated ages ranging from 2695 to 241 Ma (Table S1, Figure 7f). Among them, eight analytical spots give concentrate ages of 283 to 280 Ma and yield a mean $^{206}Pb/^{238}U$ age of 281 ± 4 Ma. One recrystallized zircon with unzoned structure (spot # 1, Figure 6e) has a much younger $^{206}Pb/^{238}U$ age of 241 ± 8 Ma, which is interpreted to represent the metamorphic age of the schist. The remaining older ages of 320 to 2695 Ma are interpreted as the ages of xenocrystic or inherited zircons.

5.2.3. Zircon Trace Elements

In the chondrite normalized REE diagram (Figure 8a), the Triassic zircons from sample 12DP1-1 exhibit high REE abundances (∑REE = 391.79–1605.02 ppm) and steep middle rare earth element (MREE)-heavy rare earth element (HREE) patterns with high $(Lu/Gd)_N$ ratios of 17.65 to 69.75, positive Ce anomalies with Ce/Ce* ratios of 20.1 to 144.5, and weak Eu anomalies with Eu/Eu* ratios of 0.43 to 0.68 (Table S2). In contrast, the pre-Triassic zircon grains display significantly low REE abundances (∑REE = 1.52–33.17 ppm) and chaotic REE patterns, without Ce and Eu anomalies, indicating that the protolith zircons may be metamorphosed through variable degrees of chemical alteration [107,108]. For the zircons with concordant Triassic U-Pb ages, their CL images, Th/U ratios, and REE patterns indicate that they are magmatic origin; therefore, the weighted mean age (230 ± 1 Ma) of these zircons are interpreted as the protolith age for sample 12DP1-1. The pre-Triassic ages are interpreted to represent the metamorphic time of xenocrystic or inherited zircons in the sample, as revealed by their unzoned or weak zoned CL images, low Th/U ratios (except for spots # 12 and # 14), and chaotic REE patterns.

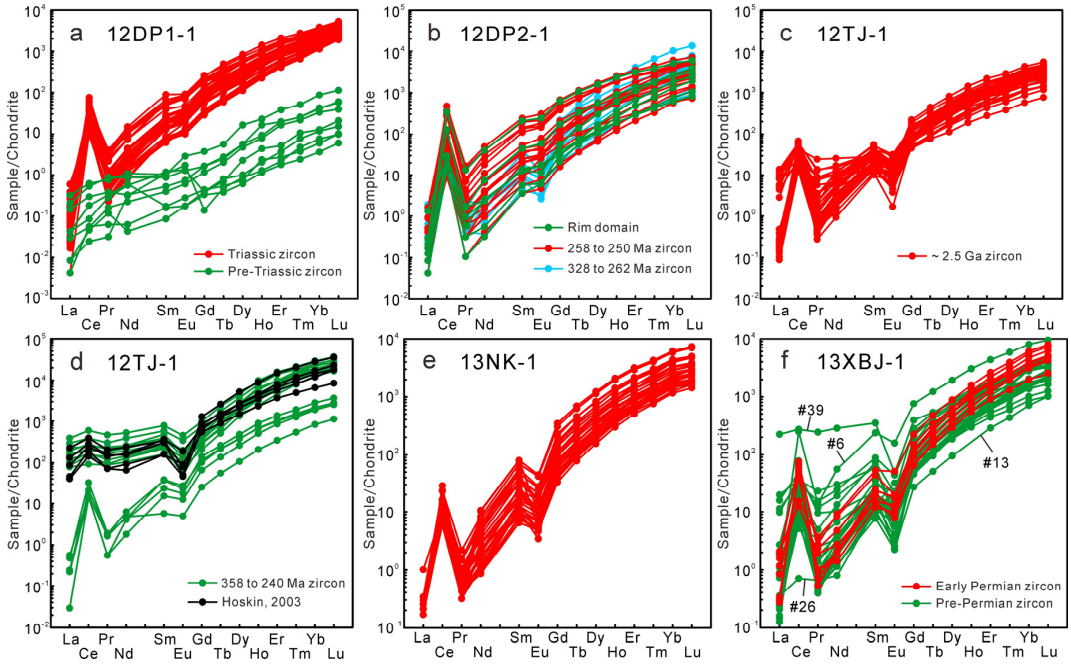

Figure 8. Chondrite-normalized REE patterns of zircons from the (**a**,**b**) gneisses, (**c**,**d**) actinolite schist, (**e**) leptynite and (**f**) hornblende-biotite schist in this study.

Based on the chondrite normalized REE patterns (Figure 8b), the pre-Triassic zircons from sample 12DP2-1 can be divided into two groups (I and II). Group-I zircons have $^{206}Pb/^{238}U$ ages of 258 to 250 Ma and exhibit HREE enrichment with $(Lu/Gd)_N$ of 8.94 to 93.98, together with pronounced positive Ce anomalies (Ce/Ce* = 34.6 to 302.3) but weak or negligible Eu anomalies (Eu/Eu* = 0.39 to 0.82) (Table S2). Group-II zircons have older $^{206}Pb/^{238}U$ ages of 328 to 262 Ma and show steeper MREE-HREE patterns with $(Lu/Gd)_N$ of 19.87 to 148.04, together with pronounced positive Ce anomalies (Ce/Ce* = 7.4–114.3) and negative Eu anomalies (Eu/Eu* = 0.08–0.27) (Table S2). The weighted mean age (254 ± 2 Ma, MSWD = 0.23) of group-I zircons (mantle-affinity zircons) is interpreted to most accurately represent the protolith age for sample 12DP2-1, whereas the older ages are interpreted to represent the magmatic or metamorphic ages of captured zircons during magma ascent because some spots were obviously made on recrystallized domains (e.g., # 28 and # 35). The rim domains show REE patterns with significant HREE enrichment ($(Lu/Gd)_N$ = 9.74–89.93), positive Ce anomalies (Ce/Ce* = 18.4–197.2) and variable Eu anomalies (Eu/Eu* = 0.32–0.81). Thus they show the nearly full inheritance in trace

elements from the protolith zircon. This, together with the high Th/U ratios, indicates that the trace element system was not significantly modified during recrystallization.

Zircons from sample TJ-1 display different REE patterns (Figure 8c,d). The REE composition of ~2.5 Ga zircons is similar to magmatic zircons showing the positive Ce (Ce/Ce* = 2.17–138.10) and negative Eu anomalies (Eu/Eu* = 0.05–0.36) and the depletion in LREEs ($(Lu/Gd)_N$ = 11.27–61.99), suggesting that the trace element system of protolith zircons was not significantly modified during post-magmatic recrystallization and metamorphism. The 358–240 Ma zircons can be divided into two types according to their CL images and REE patterns: (1) five of them (e.g., # 47) exhibit weak oscillatory zoning and magmatic REE patterns with significant HREE enrichment, positive Ce anomalies, and negative Eu anomalies (Figure 8d), and (2) ten of them are homogeneous with no CL response and are enriched in the REEs, especially the light rare earth elements (LREEs), with negative Eu anomalies but weak/negligible Ce anomalies (Figure 6d), which are similar to those of the hydrothermal zircons of Boggy Plain zoned pluton [109], indicating that these zircons are hydrothermal origin. Thus, these young ages could have resulted from post-magmatic hydrothermal events.

Zircons from sample 13NK-1 all have typical magmatic REE patterns with steeply increasing from La to Lu, positive Ce anomalies and negative Eu anomalies (Figure 8e), indicating a magmatic origin. For sample 13XBJ-1, most zircons have magmatic REE patterns with significant HREE enrichment, positive Ce anomalies and negative Eu anomalies, however, some zircons (e.g., spots # 6, # 13, # 26, and # 39) have abnormal REE patterns (Figure 8f), implying an open system process.

5.2.4. Zircon Hf Isotopes

For the Hf isotope analysis, this study selected magmatic zones and inherited/captured zircons from samples 12DP1-1, 12DP-2, 13NK-1, and 13XBJ-1, which were analyzed for U-Pb isotopic compositions. Laser spots of the Lu-Hf analyses partly or totally overlapped those of the U-Pb analyses (Figure 6). The results are listed in Table S4 and are shown in Figure 9.

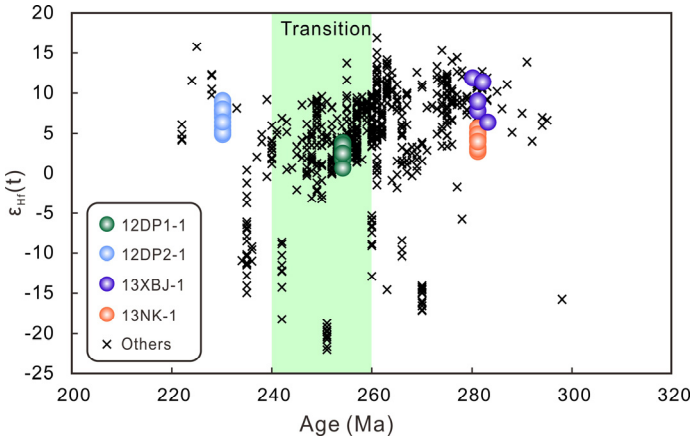

Figure 9. $\varepsilon_{Hf}(t)$ values versus ages from the Permian to the Triassic magmatic rocks along the CYS. The arrows outline the trend of zircon Hf isotopic evolution with time. The decreasing arrow illustrates an evolved trend, whereas the increasing arrow indicates a depleted trend. The green field represents the tectonic transitional period with a considerable isotopic variation. Data for other coeval magmatic rocks are from the works in [36,37,40,42–46].

Fifteen ~237 Ma primary zircons from sample 12DP-1 yield $^{176}Hf/^{177}Hf$ ratios of 0.282789–0.282902, with $\varepsilon_{Hf}(t)$ values ranging from +4.99 to +9.17, corresponding to Hf single-stage (T_{DM1}) ages ranging from 670 to 490 Ma, respectively.

$^{176}Hf/^{177}Hf$ ratios and $\varepsilon_{Hf}(t)$ values of fifteen ~254 Ma primary zircons from sample 12DP-2 are 0.282651–0.282750 and +0.75 to +3.97, respectively, with T_{DM1} ages of 850–729 Ma.

Fifteen magmatic zircon grains from sample 13NK-1 show intensive Hf isotopic compositions, with $^{176}Hf/^{177}Hf$ ratios of 0.282698–0.282781, $\varepsilon_{Hf}(t)$ values of +2.87 to +5.84, and T_{DM2} ages of 1090–902 Ma.

Twenty zircon Hf spot analyses from sample 13XBJ-1 were obtained, which included five ~281 Ma primary zircons that have $^{176}Hf/^{177}Hf$ ratios of 0.282801–0.282961, $\varepsilon_{Hf}(t)$ values of +6.56 to +12.04, and T_{DM1} ages of 650–426 Ma. The remaining fifteen inherited/captured zircons with U-Pb ages of 2695–320 Ma from this sample yield $^{176}Hf/^{177}Hf$ ratios of 0.281314–0.282949, with $\varepsilon_{Hf}(t)$ values ranging from −5.49 to +15.48.

6. Discussion

6.1. The KYTM and HLTM Geochronology Revisited

6.1.1. The KYTM

As mentioned above, although there have been several controversial views regarding the age, division scheme, and tectonic attributes of the KYTM, recent research has indicated that these rocks are not a "group" in the stratigraphic sense, but represent a tectonic mélange, mixed by Mesoarchean gneisses, Neoarchean supracrustal rocks, metamorphosed Proterozoic sediment rocks, and late Permian meta-volcanic and meta-sedimentary rocks [38,41,48,80]. Precisely geochronological study on the zircons from the samples 12TJ-1, 12DP1-1, and 12DP2-1 provided new insights into the age of the KYTM.

Our new zircon U-Pb data indicate that the protolith of actinolite schist (sample 12TJ-1) from the Tongjiatun Formation was formed during the Paleoproterozoic, with a well-defined upper intercept age of 2441 ± 15 Ma and a $^{207}Pb/^{206}Pb$ weighted mean age of 2443 ± 20 Ma. The sample also contains some xenocrystic or inherited zircons which yielded an upper intercept age of 2570 ± 24 Ma and a $^{207}Pb/^{206}Pb$ weighted mean age of 2572 ± 36 Ma, and passed through multiple superposition of hydrothermal activities during 372–264 Ma. In terms of location, the present study area is considered to mark the boundary between the NCC and eastern CAOB. Therefore, the actinolite schist, in conjunction with previously identified ~2.5 Ga tonalitic mylonite and amphibolite [79,80], suggests that some components of the KYTM were probably originally part of the NCC, in which widespread ~2.5 Ga ages have been reported [110].

The data also demonstrate that the protolith of hornblende biotite plagioclase gneiss (sample 12DP2-1) formed during the late Permian (254 ± 2 Ma), which is consistent with previously reported late Permian dacite, high-Mg andesite, albite–actinolite schist, amphibolite, and diopside granulite from the KYTM [38,41,48,79]. Furthermore, magmatic zircons from the hornblende epidote plagioclase gneiss (sample 12DP1-1) yielded a weighted mean age of 230 ± 1 Ma, suggesting that the protolith formed during the Late Triassic. This newly identified gneiss suggests that the formation of the KYTM could not earlier than the Late Triassic.

Based on the above new geochronological data and previous results, we infer that the KYTM mainly formed from the amalgamation of Mesoarchean–Paleoproterozoic metamorphic rocks, Proterozoic meta-sediment rocks, Late Permian meta-volcanic and meta-sedimentary rocks, as well as Late Triassic meta-volcanic rocks that were probably juxtaposed after the Late Triassic era.

6.1.2. The HLTM

The HLTM was once considered to be a true stratigraphic succession that formed during the Early Palaeozoic [81–84]. Despite the fact that the age of the HLTM has long been a subject of extensive studies [28,81–84], no consensus of opinion on the protolith ages has been reached due to a lack of detailed geochronological data. LA-ICP-MS zircon U-Pb dates for the leptynite from the Huangyingtun Formation and the schist from the Xiaosan'gedingzi Formation define weighted mean ages of 281 ± 2 Ma and 281 ± 4 Ma, respectively, which are consistent with the maximum depositional age (287 ± 6 Ma) of the protolith for a pelitic schist from the Huangyingtun Formation [28]. Conversely, zircon U-Pb age

results of schist samples and a felsic dike intruded into the schists from the Yantongshan area indicate that the clastic sediments of the Yantongshan Complex, which is a part of the HLTM, were deposited between 237 and 217 Ma [111]. Therefore, we infer that the HLTM consists of at least the Early Permian Huangyingtun and Xiaosan'gedingzi complexes and Middle–Late Triassic Yantongshan Complex. The formation of the HLTM thus was not earlier than the Late Triassic, and not during the Early Paleozoic as previously believed.

6.2. Petrogenetic Implications

6.2.1. Assessment of Element Mobility

Given the metamorphism and alteration the above Permo–Triassic metamorphic rocks have undergone, element mobility should be evaluated prior to any petrogenetic discussions. Polat et al. (2002) [112] have reported that meta-volcanic rocks with LOI values higher than 6 wt% were subjected to variable alteration. The studied samples have lower LOI values (0.95–4.35 wt%, except sample 12DP1-2 with 11.65 wt% LOI value) indicating effects of alteration. The significantly high LOI and CaO content (18.60 wt%) of sample 12DP1-2 definitively points to strong alteration; therefore, this sample will not be used in the following discussion. Most samples have coherent patterns in the primitive mantle-normalized spider diagram and chondrite-normalized REE diagram (Figure 5), confirming the preservation of the original signatures of HFSEs and REEs. In the following discussion, Ti, Fe, Al, P, transition metals, REEs, and HFSEs, which were considered to be relatively immobile during greenschist- to amphibolite-facies metamorphism [113–117], were selected to discuss the petrogenesis of protoliths.

6.2.2. Crustal Contamination of the Basaltic Rocks

As mantle-derived magmas could be contaminated by upper crustal material during ascent or emplacement, understanding the effects of crustal contamination on basaltic rocks is important. Xenocrystic/captured zircons were identified from all the basaltic rocks (Figure 5), thereby providing evidence of crustal contamination or assimilation during magmatism. However, crustal contamination or magma mixing en route can be ignored based on the following observations; (1) the absence of positive Zr-Hf anomalies in the studied basaltic samples rules out significant crustal contamination because Zr and Hf are enriched in crustal materials [118]; (2) the studied basaltic samples have Ce/Pb (14.40–40.61) and Nb/U (8.55–27.76) ratios that are substantially higher than those of continental crust (Ce/Pb = 3.91 and Nb/U = 6.15) [118,119], indicating limited crustal contamination; (3) the low Th/La (0.06–0.20) and Th/Ce (0.03–0.10) ratios of the basaltic samples suggest that crustal contamination played an insignificant role during the magma evolution because continental crust has relatively high Th/La (~0.3) and Th/Ce (~0.15) ratios [120,121], while mantle-derived magmas have low Th/Ce (0.02–0.05) and Th/La (~0.12) ratios [118]. In conclusion, crustal contamination of the studied basaltic samples is negligible, and the protoliths of the metamorphic rocks were therefore likely derived from mantle sources.

6.2.3. Origin of the Early Permian Protoliths of the Metamorphic Rocks from the HLTM

Petrographic and geochemistry investigations of the Early Permian 13XBJ schists reveal that the protoliths of these rocks are basalts. They plot in the alkali basalt field in the Zr/TiO_2 vs. Nb/Y diagram (Figure 4b), with high concentrations of Zr (175.40–216.82 ppm), Nb (24.31–42.36 ppm), Y (25.48–45.20 ppm), Th (4.09–7.13 ppm), Hf (4.96–7.62 ppm), TiO_2 (2.74–3.67 wt%), and P_2O_5 (0.23–2.06 wt%). Traditionally, ultramafic lithologies including peridotite, carbonated peridotite, hornblendite, and silica-deficient pyroxenite/eclogite are considered to be possible mantle sources of alkali basalts [122–124].

As is well known that the addition of CO_2 diminishes the SiO_2 content of partial melts of peridotite [125], carbonated peridotite-derived melts generally exhibit significantly low SiO_2

contents [122], which cannot explain the SiO_2 contents (43.87–48.29 wt%) of the 13XBJ samples. Thus, the protoliths of 13XBJ samples could not be generated from carbonated peridotite. For melts from silica-deficient pyroxenite/eclogite, they would generate magmas with relatively higher SiO_2 (>55%) and Ni/MgO ratios [124,126] than those of the 13XBJ samples. This precludes the possibility that they were derived from the partial melting of silica-deficient pyroxenite/eclogite. The 13XBJ samples have SiO_2 contents of 43.87% to 48.29%, relatively lower CaO contents (11.08–13.67 wt%) and CaO/Al_2O_3 ratios, which are similar to those of peridotite-derived melts [122,127]. However, the 13XBJ samples show significantly higher TiO_2 and alkali contents, indicating that the only mantle peridotite cannot be their direct source. The high Ti and alkali contents for a mantle source imply the presence of a metasomatic lithology, such as hornblendite. As illustrated in Figure 10, the basaltic samples plot between peridotite- and hornblendite-derived melts, suggesting a combined source that is composed of hornblendite and peridotite [128–132]. In summary, the protoliths of 13XBJ schists from the HLTM were probably derived from partial melting of the combined sources, with both peridotite and hornblendite as the metasomatized mantle.

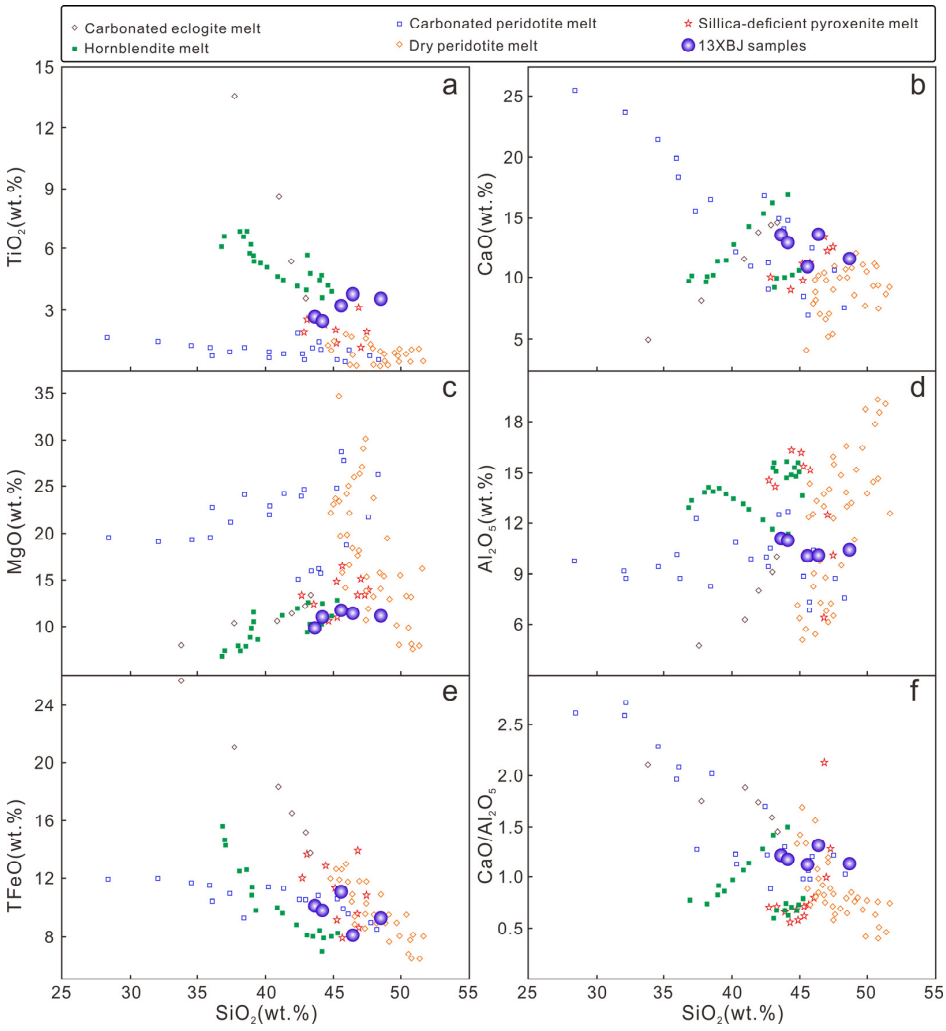

Figure 10. Plots of SiO_2 versus TiO_2 (**a**), CaO (**b**), MgO (**c**), Al_2O_3 (**d**), TFeO (**e**), and CaO/Al_2O_3 (**f**) for the 13XBJ samples. Data of different experimental alkali melt compositions are from the works in [128–132].

The coeval felsic rocks (13NK leptynite samples) are characterized by relatively higher SiO_2 (63.22–68.92 wt%) and lower MgO (1.19–2.31 wt%) concentrations, implying a parental magma of protoliths sourced from lower continental crust. This hypothesis is further supported by the following

observations; (1) the leptynites are enriched in Nd and Rb, and depleted in Nb, Ta, Ti, and P, which is typical of crustal materials [118]; (2) these rocks have remarkably low Mg# values (34–48) and transition metal (e.g., Cr, Ni, and Co) concentrations (Table S3), as well as positively inclined REE patterns, with high HREE concentrations and weak HREE fractionation (Figure 5b); (3) their incompatible element ratios, such as Ti/Y (74.54–118.26; average = 95.25) and Ti/Zr (18.19–29.45; average = 28.23) are consistent with magma derived from the continental lower crust [118,133–135]. These characteristics, together with the positive correlation between Pb and SiO_2 contents, negative correlation between P_2O_5 and SiO_2 contents (Figure 11a,b), and absence of Al-rich minerals, suggest that the protoliths of leptynites are similar to highly fractionated I-type granite [136–141]. Moreover, data for the leptynite samples plot mainly in the field of highly fractionated I-type granite in the (10,000 × Ga/Al) and (FeO/MgO) vs. (Zr + Nb + Ce + Y) diagrams (Figure 11c,d). Crucially, the leptynite samples yield positive εHf(t) values (+2.87 to +5.84) and primarily Meso–Neoproterzoic T_{DM2} ages (1090–902 Ma), implying a parental magma sourced from Meso–Neoproterozoic accreted lower continental crust, similar to the mechanism proposed for coeval felsic rocks in the CYS [74,142].

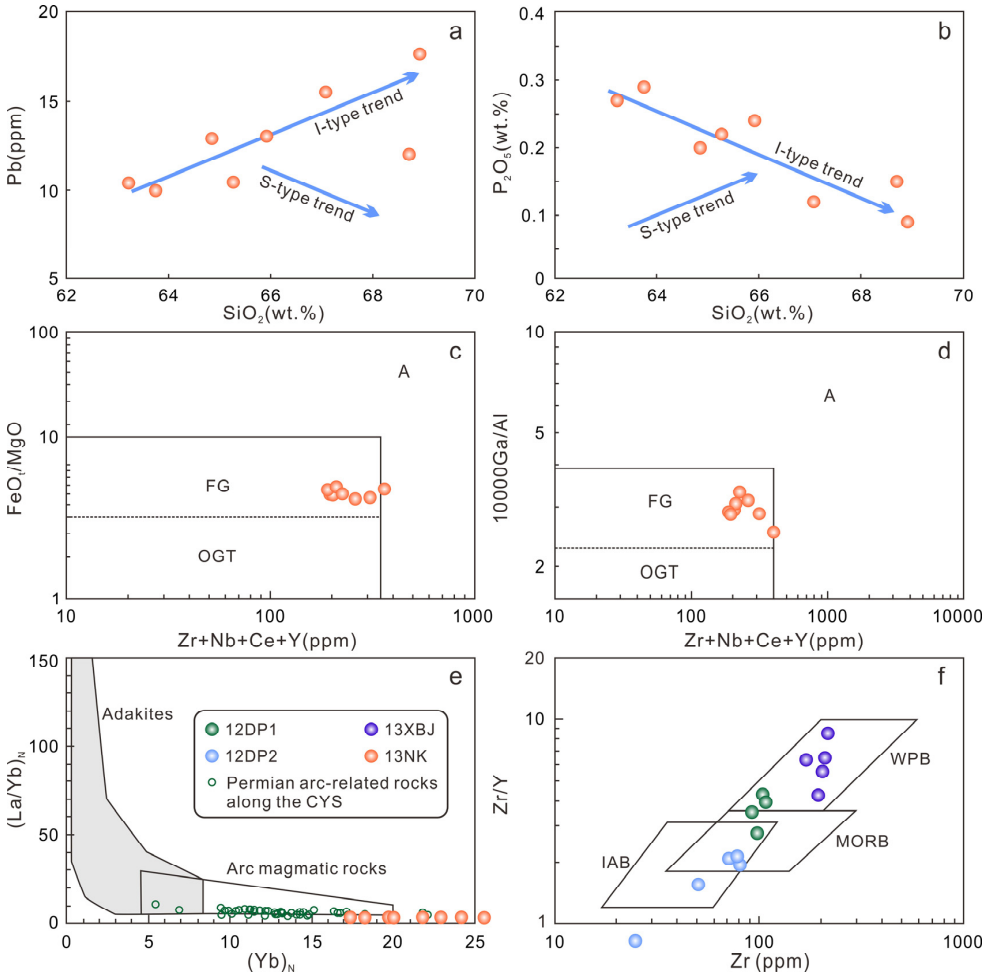

Figure 11. (**a**,**b**) Pb versus SiO_2 diagram and P_2O_5 versus SiO_2 diagram showing that the felsic rocks follow the trend of I–type [136]. (**c**,**d**) FeO_t/MgO, 10,000 Ga/Al versus (Zr + Nb + Ce + Y) discrimination diagrams to show the genetic characteristics of the felsic rocks [143]. (**e**) $(La/Yb)_N$ versus Yb_N diagram for the felsic rocks [144]. (**f**) Zr/Y versus Zr (ppm) diagram for the basaltic rocks [145]. Data of Permian arc-related rocks along the CYS are from the works in [35–37,40,142].

6.2.4. Origin of the Late Permian and Late Triassic Protoliths of the Metamorphic Rocks from the KYTM

Petrographic, geochemistry, and field investigations of the gneisses (12DP1 and 12DP2 samples) from the KYTM reveal that the protoliths of these rocks are subalkaline basaltic volcanic rocks. They are characterized by low MgO contents (4.05–7.86% wt%), Mg# values (45–75), and amounts of Cr (36.69–117.09 ppm), Co (16.72–40.65 ppm), and Ni (20.68–39.78 ppm), which suggest that they were derived from more evolved mafic magmas and experienced some degree of the fractional crystallization of clinopyroxene and olivine [146]. The presence of negative Ti and P anomalies indicates that this magma experienced the fractional crystallization of Ti-bearing phases and apatite (Figure 5d). Moreover, the 12DP2 samples have more abundant REE concentrations and show negative Eu anomalies that indicate plagioclase fractionation (Figure 5a), as plagioclase has nearly constant partition coefficients for REE ($D \approx 0.1$), except Eu.

The studied basaltic samples from the KYTM have positive zircon $\varepsilon Hf(t)$ values (+3.6 to +4.4) and T_{DM1} ages ranging from 850 to 490 Ma, indicating that the primary magmas of the protoliths of the gneisses were probably generated by the partial melting of a juvenile depleted lithospheric mantle. These samples display relative enrichment in LREEs and LILEs, and a depletion of HFSEs, implying that the magma source had been metasomatized by subducted slab-derived fluids/melts, or contaminated by a massive amount of crustal material during its magmatic migration [147,148]. However, the above interpretations suggest that crustal contamination of the studied basaltic samples is negligible. Consequently, the primary magmas that formed the protoliths of the gneisses from the KYTM were probably derived from partial melting of a depleted lithospheric mantle that was metasomatized by subducted slab-derived fluids.

6.3. Tectonic Implications for the PAO Regime and MO Regime

6.3.1. Permo–Triassic Tectonic Evolution of the Eastern Segment of PAO

A majority of reconstructions based on integrated analyses of magmatic and sedimentary records suggest that the Songnen Block have been attached to the northern margin of the NCC during Permian to Triassic time due to closure of the PAO [35–54]. However, the precise time of the final closure of eastern segment of the PAO along the CYS remains a disputable issue, as vital outcrops are poor and were strongly deformed.

In this study, synthesizing studies on metamorphic rocks from the Kaiyuan and Hulan tectonic mélanges are applied to constrain the final closure of the PAO along the CYS. The protoliths of Early Permian leptynite samples from the HLTM are silicic volcanic rocks. These rocks are enriched in LILEs with respect to the HFSEs, indicating that the magmas were generated in subduction-related environment or their protolith was produced in a subduction context [149,150]. In the $(La/Yb)_N$-$(Yb)_N$ diagram, they plot within the typical arc-rock field (Figure 11e), similar to previously reported Early to Middle Permian Andean-type intermediate to felsic volcanic rocks from the Daheshen and Panling formations in northern Liaoning and central Jilin provinces [35–37,42,44,45,142]. Therefore, the development of the northern margin of the NCC was mainly controlled by subduction of the Plaeo-Asian oceanic plate during the Early to Middle Permian. As mentioned earlier, the protoliths of Late Permian gneiss samples from the KYTM are basaltic volcanic rocks. The most significant characteristic of these rocks is their depletion in HFSEs (e.g., Nb, Ta, and Ti), providing evidence of arc affinities [151]. All these samples plot within the volcanic arc basalt/active continental margin basalt field in the Zr/Y-Zr discrimination diagram (Figure 11f). Additionally, a quantity of Late Permian arc-related igneous rocks, such as the Daheishan, Seluohe, Wudaogou, and Guanmenzuizi volcanic rocks, were also identified along the CYS [35,40]. Therefore, we conclude that the Paleo-Asian oceanic plate was still subducting during the Late Permian.

The studied 12DP1 samples from the KYTM yield a protolith age of 231 Ma, suggesting that the basaltic rocks were formed during the Late Triassic. These rocks, together with

ultramafic-mafic intrusive rocks, coeval I- and A-type granitoids, and A-type rhyolites along the CYS [36,152,153], constitute a bimodal assemblage typical of extensional environments. This inference is also demonstrated by the presence of Late Triassic molasse deposit in central Jilin Province, which delineates the transition from orogenic uplift to post-orogenic extension [49,52,69]. Consequently, the continent-continent collision between the Songnen Block and NCC, that is, the final closure of the PAO in the northern Liaoning and central Jilin provinces occurred during the Early to Middle Triassic. This proposal was further supported by the following conclusive geological evidence. For example, the Early Triassic (ca. 250 Ma) high-Mg andesites from the Seluohe and Kaiyuan area, along with coeval bimodal igneous rock association, suggesting an extensional environment caused by break-off of the subducting slab during the initial stages of continental collision [38,41]. In addition, the increasingly evolved zircon εHf(t) values from the Early to Late Permian suggest an advancing oceanic subduction regime where more old crustal materials were involved, while the juvenile isotope signatures for the Middle to Late Triassic magmatic rocks along the CYS can be attributed to the involvement of asthenospheric mantle-derived magmas in a subsequent extensional setting (Figure 9). Therefore, a complex tectonic regime transition from compressional subduction to extensional post-collisional settings must have occurred during the transitional period at the end Permian to the latest Middle Triassic. Moreover, a large amount of Early–Middle Triassic syn-collisional granitoids, such as the Dayushan, Liushugou, Jianpingzhen, and Fudongzhen plutons [36,37,39,42,43,46], are widely distributed within the CYS. All these lines of evidence, in conjunction with the absence of Late Triassic marine sediments [46], suggest that the final closure of the PAO should occurred during the Early to Middle Triassic.

6.3.2. Implications for the Tectonic Evolution of the MO

Recent studies suggest that the late Paleozoic–early Mesozoic tectonic evolution between the Jiamusi and Songnen blocks was related to the development of the MO [55–68]; however, the formation time of the ocean is still ambiguous, as this region is overprinted by several Paleozoic to Mesozoic Paleo-Asian and circum-Pacific tectonic regimes [23,24,26,39,42,46,69,76]. A number of studies suggest that the ocean existed during the Permian [55–57]. In contrast, some researchers have recently proposed that the MO was a short-lived ocean that existed during the Middle Triassic–Early Jurassic [62].

The studied 13XBJ samples from the HLTM provide new insights on the tectonic evolution of the MO. Geochronological and geochemical data presented in this study indicate that the basaltic protoliths of these rocks can be divided into alkali basalt which formed during the Early Permian (~281 Ma). These rocks are markedly different from the Permian subduction-related igneous rocks distributed in the CYS [35–37,40,42,45], but rather display geochemical characteristics similar to those of OIB, thus precluding the possibility that they formed in a middle ocean ridge or a magmatic arc setting. However, whether they formed in an ocean island or a continental rifting setting are still ambitious.

As mentioned earlier, the alkali basaltic rock (Sample 13XBJ-1) contains abundant xenocrystic/inherited zircons with ages ranging from 320 Ma to 2695 Ma. The large time gap between the rock-forming age and the oldest xenocrystic/inherited zircons excludes the possibility that the alkali basalts formed as an oceanic crust. The presence of abundant xenocrystic/inherited zircons, when coupled with OIB signature of basalt protoliths, favours eruption in a rift environment [64,65]. It therefore seems that the 13XBJ basaltic rocks most likely formed in a continental rift setting, similar to a previously reported ~275 Ma OIB-type blueschist from the Heilongjiang Complex [64,65]. The formation of these rocks were proposed to be related to the beginning of a continental rifting event, which resulted in the formation of the MO until sometime after the Early Permian [65–67]. In addition, the occurrence of Triassic passive continental margin sediments and bimodal igneous rock association lead Long et al. (2020) [62] proposed that the MO could have opened along the Jiamusi-Mudanjiang Fault during the Middle Triassic, due to the north–south trending compression caused by the final closure of the PAO.

It is noteworthy that the continental-rift-related rocks (13XBJ samples) from the HLTM are much further away from the Jiamusi-Mudanjiang Fault, which is considered to represent the remains of the MO, in contrast to the coeval blueschists from the Heilongjiang Complex. A comprehensive analysis of Paleozoic–Mesozoic magmatism within the Songnen, Jiamusi, and Khanka massifs imply that at least two stages of strike slip faulting produced by the Dunhua-Mishan Fault, during the Middle Permian–Early Triassic and Middle–Late Jurassic, resulted in a total offset of ~400 km [154]. Therefore, we conclude that the continental-rift related basaltic rocks (13XBJ samples) originated from a position that close to the Dunhua-Mishan Fault, and were later carried to the current position.

7. Conclusions

On the basis of field observations, zircon U-Pb geochronological and Hf isotopic analyses, and whole-rock major and trace element analyses presented above, we can draw the following conclusions.

(1) The protoliths of metamorphic rocks from the KYTM and HLTM were volcanic rocks that formed during the Permian–Triassic and Mesoarchean–Paleoproterozoic. The KYTM and HLTM are considered to be probably juxtaposed after the Late Triassic.

(2) The Early Permian protoliths of chloritic hornblende biotite schists from the HLTM were probably derived from partial melting of the combined sources, with both peridotite and hornblendite as the mantle lithologies, while the coeval felsic rocks were generated from a Meso–Neoproterozoic accreted lower continental crust.

(3) The primary magmas that formed the Late Permian and Late Triassic protoliths of the gneisses from the KYTM were probably derived from partial melting of a depleted lithospheric mantle that was metasomatized by subducted slab-derived fluids/melts.

(4) The identification of Permian subduction-related rocks, combined with the Late Triassic bimodal igneous rock association, indicates that the PAO closed during the Early–Middle Triassic. The formation of the Early Permian basaltic rocks from the HLTM probably formed in a continental rifting setting that was related to the formation of the MO.

Supplementary Materials: The following are available online at http://www.mdpi.com/2075-163X/10/9/836/s1, Table S1: LA-ICP-MS zircon U-Pb data for the metamorphic rocks in this study, Table S2: LA-ICP-MS zircon trace element data for the metamorphic rocks in this study, Table S3: Major (wt%) and trace (ppm) elements of the metamorphic rocks in this study, Table S4: Lu-Hf isotopic data of zircons from the metamorphic rocks in this study.

Author Contributions: Conceptualization, Z.H., Sampling and Experiments, Z.S., W.Z., Z.H., G.L., and L.G., Data analysis and Figures, J.L., Q.D., and W.Z., Writing—Original Draft Preparation, Z.S., Writing—Review and Editing, Z.H. and J.L., All authors have read and agreed to the published version of the manuscript.

Funding: This research was funded by the Natural Science Foundation of Shandong Province (Grant ZR2019PD001), the Taishan Scholar Talent Team Support Plan for Advantaged & Unique Discipline Areas, the Youth Innovation Team Development Plan of Universities in Shandong Province (Deep-Time Paleoclimate and Sedimentary Mineralization), and the SDUST Research Fund (Grant 2015TDJH101).

Acknowledgments: Thanks go to Yujing Peng, Wenlong Zhao, Pengfei Wei, and Zhiping Guo for their assistance with field work. We acknowledge Yuanku Meng and Songjie Wang for insightful discussion concerning interpretation of the geochemical data. We are also grateful to the academic editor and anonymous reviewers, whose constructive suggestions greatly improved our manuscript.

Conflicts of Interest: The authors declare no conflict of interest.

References

1. Hsü, K. The principles of mélanges and their bearing on the Franciscan–Knoxville Paradox. *Geol. Soc. Am. Bull.* **1968**, *79*, 1063–1074. [CrossRef]
2. Rast, N.; Horton, J.W., Jr. Mélanges and olistostromes in the Appalachians of the United States and mainland Canada: An assessment. *Spec. Pap. Geol. Soc. Am.* **1989**, *228*, 1–15.
3. Şengör, A.M.C. The repeated rediscovery of mélanges and its implications for the possibility and the role of objective evidence in the scientific enterprise. *Spec. Pap. Geol. Soc. Am.* **2003**, *373*, 385–446.

4. Robertson, A.H.F.; Ustaömer, T. Role of tectonic-sedimentary melange and Permian–Triassic cover units, central southern Turkey in Tethyan continental margin evolution. *J. Asian Earth Sci.* **2011**, *40*, 98–121. [CrossRef]
5. Kusky, T.M.; Windley, B.F.; Safonova, I.; Wakita, K.; Wakabayashi, J.; Polat, A.; Santosh, M. Recognition of ocean plate stratigraphy in accretionary orogens through earth history: A record of 3.8 billion years of sea floor spreading, subduction, and accretion. *Gondwana Res.* **2013**, *24*, 501–547. [CrossRef]
6. Wang, J.P.; Kusky, T.; Polat, A.; Wang, L.; Deng, H.; Wang, S.J. A late Archean tectonic mélange in the Central Orogenic Belt, North China Craton. *Tectonophysics* **2013**, *608*, 929–946. [CrossRef]
7. Wang, J.P.; Li, X.W. Geology of a Neoarchean suture: Evidence from the Zunhua ophiolitic mélange of the Eastern Hebei Province, North China Craton. *Geol. Soc. Am. Bull.* **2019**, *131*, 1943–1964. [CrossRef]
8. Jahn, B. The Central Asian Orogenic Belt and growth of the continental crust in the Phanerozoic. *Geol. Soc. Lond. Spec. Publ.* **2004**, *226*, 73–100. [CrossRef]
9. Li, J.Y. Permian geodynamic setting of northeast China and adjacent regions: Closure of the Paleo-Asian Ocean and subduction of the Paleo-Pacific plate. *J. Asian Earth Sci.* **2006**, *26*, 207–224. [CrossRef]
10. Xiao, W.J.; Windley, B.; Sun, S.; Li, J.L.; Huang, B.C.; Han, C.M.; Yuan, C.; Sun, M.; Chen, H.L. A tale of amalgamation of three Permo–Triassic collage systems in Central Asia: Oroclines, sutures, and terminal accretion. *Annu. Rev. Earth Planet. Sci.* **2015**, *43*, 477–507. [CrossRef]
11. Liu, Y.J.; Li, W.M.; Feng, Z.Q.; Wen, Q.B.; Neubauer, F.; Liang, C.Y. A review of the Paleozoic tectonics in the eastern part of Central Asian Orogenic Belt. *Gondwana Res.* **2017**, *43*, 123–148. [CrossRef]
12. Safonova, I.; Kotlyarov, A.; Krivonogov, S.; Xiao, W.J. Intra-oceanic arcs of the Paleo-Asian Ocean. *Gondwana Res.* **2017**, *50*, 167–194. [CrossRef]
13. Safonova, I. Juvenile versus recycled crust in the Central Asian Orogenic Belt: Implications from ocean plate stratigraphy, blueschist belts and intra-oceanic arcs. *Gondwana Res.* **2017**, *47*, 6–27. [CrossRef]
14. Han, Z.Z.; Song, Z.G.; Han, C.; Zhong, W.J.; Han, M.; Yan, J.L.; Liu, H.; Du, Q.X.; Gao, L.H.; Li, J.J. U–Pb ages and Hf isotopic composition of zircons and whole rock geochemistry of volcanic rocks from the Fangniugou area: Implications for early–middle Paleozoic tectonic evolution in Jilin Province, NE China. *J. Miner. Petrol. Sci.* **2018**, *113*, 10–23. [CrossRef]
15. Han, Z.Z.; Liu, H.; Song, Z.G.; Zhong, W.J.; Han, C.; Han, M.; Du, Q.X.; Gao, L.H.; Li, J.J.; Yan, J.L. Geochronology, geochemistry, and tectonic implications of upper Silurian–Lower Devonian meta-sedimentary rocks from the Jiangyu group in eastern Jilin Province, Northeast China. *Can. J. Earth Sci.* **2018**, *55*, 490–504. [CrossRef]
16. Zhou, J.B.; Wilde, S.A.; Zhao, G.C.; Han, J. Nature and assembly of microcontinental blocks within the Paleo-Asian Ocean. *Earth-Sci. Rev.* **2018**, *186*, 76–93. [CrossRef]
17. Du, Q.X.; Han, Z.Z.; Shen, X.L.; Han, C.; Han, M.; Song, Z.G.; Gao, L.H.; Liu, H.; Zhong, W.J.; Yan, J.L. Zircon U–Pb geochronology and geochemistry of the post-collisional volcanic rocks in eastern Xinjiang Province, NW China: Implications for the tectonic evolution of the Junggar terrane. *Int. Geol. Rev.* **2018**, *60*, 339–364. [CrossRef]
18. Du, L.; Long, X.P.; Yuan, C.; Zhang, Y.Y.; Huang, Z.Y.; Sun, M.; Zhao, G.C.; Xiao, W.J. Early Paleozoic Dioritic and Granitic Plutons in the Eastern Tianshan Orogenic Belt, NW China: Constraints on the Initiation of a Magmatic Arc in the Southern Central Asian Orogenic Belt. *J. Asian Earth Sci.* **2018**, *153*, 139–153. [CrossRef]
19. Du, L.; Long, X.P.; Yuan, C.; Zhang, Y.Y.; Huang, Z.Y.; Wang, X.Y.; Yang, Y.H. Mantle contribution and tectonic transition in the Aqishan-Yamansu Belt, Eastern Tianshan, NW China: Insights from geochronology and geochemistry of Early Carboniferous to Early Permian felsic intrusions. *Lithos* **2018**, *304–307*, 230–244. [CrossRef]
20. Du, L.; Long, X.P.; Yuan, C.; Zhang, Y.Y.; Huang, Z.Y.; Sun, M.; Xiao, W.J. Petrogenesis of late paleozoic diorites and a-type granites in the central Eastern Tianshan, NW China: Response to post-collisional extension triggered by slab breakoff. *Lithos* **2018**, *318–319*, 47–59. [CrossRef]
21. Song, Z.G.; Han, C.; Liu, H.; Han, Z.Z.; Yan, J.L.; Zhong, W.J.; Gao, L.H.; Du, Q.X.; Han, M.; Li, J.J. Early-Middle Ordovician intermediate-mafic and ultramafic rocks in central Jilin Province, NE China: Geochronology, origin, and tectonic implications. *Miner. Petrol.* **2019**, *113*, 393–415. [CrossRef]
22. Windley, B.F.; Alexeiev, D.; Xiao, W.J.; Kröner, A.; Badarch, G. Tectonic models for accretion of the Central Asian Orogenic belt. *J. Geol. Soc.* **2007**, *164*, 31–47. [CrossRef]

23. Xu, W.L.; Pei, F.P.; Wang, F.; Meng, E.; Ji, W.Q.; Yang, D.B.; Wang, W. Spatial–temporal relationships of Mesozoic volcanic rocks in NE China: Constraints on tectonic overprinting and transformations between multiple tectonic regimes. *J. Asian Earth Sci.* **2013**, *74*, 167–193. [CrossRef]
24. Wilde, S.A.; Zhou, J.B. The late Paleozoic to Mesozoic evolution of the eastern margin of the Central Asian Orogenic Belt in China. *J. Asian Earth Sci.* **2015**, *113*, 909–921. [CrossRef]
25. Zhou, Z.Z.; Li, S.Z.; Guo, L.L.; Li, X.Y.; Jiang, Z.X.; Liu, Y.J.; Li, Y.; Wang, G.Z.; Lan, H.Y.; Guo, R.H.; et al. Palaeomagnetic assessment of tectonic rotation in Northeast Asia: Implications for the coupling of intracontinental deformation and mantle convection. *Int. Geol. Rew.* **2020**. [CrossRef]
26. Han, Z.Z.; Ren, X.; Schertl, H.P.; Li, X.P.; Song, Z.G.; Du, Q.X.; Han, C.; Zhong, W.J.; Gao, L.H. Zircon U-Pb-Hf isotopes and geochemistry of Jurassic igneous rocks from the southern Zhangguangcai Range, NE China: Constraints on magmatism, petrogenesis and tectonic implications. *Int. Geol. Rew.* **2019**. [CrossRef]
27. Han, Y.G.; Zhao, G.C. Final amalgamation of the Tianshan and Junggar orogenic collage in the southwestern Central Asian Orogenic Belt: Constraints on the closure of the Paleo-Asian Ocean. *Earth-Sci. Rev.* **2018**, *186*, 129–152. [CrossRef]
28. Wu, F.Y.; Zhao, G.C.; Sun, D.Y.; Wilde, S.A.; Yang, J.H. The Hulan Group: Its role in the evolution of the Central Asian Orogenic Belt of NE China. *J. Asian Earth Sci.* **2007**, *30*, 542–556. [CrossRef]
29. Lin, W.; Faure, M.; Nomade, S.; Shang, Q.H.; Renne, P.R. Permian–Triassic amalgamation of Asia: Insights from northeast China sutures and their place in the final collision of north China and Siberia. *C. R. Geosci.* **2008**, *340*, 190–201. [CrossRef]
30. Xiao, W.J.; Windley, B.; Huang, B.C.; Han, C.M.; Yuan, C.; Chen, H.L.; Sun, M.; Sun, S.; Li, J.L. End-Permian to mid-Triassic termination of the accretionary processes of the southern Altaids: Implications for the geodynamic evolution, Phanerozoic continental growth and metallogeny of Central Asia. *Int. J. Earth Sci.* **2009**, *98*, 1189–1217. [CrossRef]
31. Zhao, P.; Chen, Y.; Xu, B.; Faure, M.; Shi, G.; Choulet, F. Did the Paleo-Asian Ocean between North China Block and Mongolia block exist during the late Paleozoic? First paleomagnetic evidence from central-eastern Inner Mongolia, China. *J. Geophys. Res. Solid Earth* **2013**, *118*, 1873–1894. [CrossRef]
32. Xu, B.; Zhao, P.; Wang, Y.Y.; Liao, W.; Luo, Z.W.; Bao, Q.Z.; Zhou, Y.H. The pre-Devonian tectonic framework of Xing'an-Mongolia orogenic belt (XMOB) in north China. *J. Asian Earth Sci.* **2015**, *97*, 183–196. [CrossRef]
33. Chen, Y.; Zhang, Z.C.; Li, K.; Yu, H.F.; Wu, T.R. Detrital zircon U–Pb ages and Hf isotopes of Permo-Carboniferous sandstones in central Inner Mongolia, China: Implications for provenance and tectonic evolution of the southeastern Central Asian Orogenic Belt. *Tectonophysics* **2016**, *671*, 183–201. [CrossRef]
34. Li, S.; Wilde, S.A.; He, Z.J.; Jiang, X.J.; Liu, R.Y.; Zhao, L. Triassic sedimentation and post accretionary crustal evolution along the Solonker suture zone in Inner Mongolia, China. *Tectonics* **2014**, *33*, 960–981. [CrossRef]
35. Cao, H.H.; Xu, W.L.; Pei, F.P.; Guo, P.Y.; Wang, F. Permian tectonic evolution of the eastern section of the northern margin of the North China Plate: Constraints from zircon U–Pb geochronology and geochemistry of the volcanic rocks. *Acta Petrol. Sin.* **2012**, *28*, 2733–2750. (In Chinese)
36. Cao, H.H.; Xu, W.L.; Pei, F.P.; Wang, Z.W.; Wang, F.; Wang, Z.J. Zircon U–Pb geochronology and petrogenesis of the Late Paleozoic–Early Mesozoic intrusive rocks in the eastern segment of the northern margin of the North China Block. *Lithos* **2013**, *170–171*, 191–207. [CrossRef]
37. Wang, Z.J.; Xu, W.L.; Pei, F.P.; Wang, Z.W.; Li, Y.; Cao, H.H. Geochronology and geochemistry of middle Permian-Middle Triassic intrusive rocks from central-eastern Jilin Province, NE China: Constraints on the tectonic evolution of the eastern segment of the Paleo-Asian Ocean. *Lithos* **2015**, *238*, 13–25. [CrossRef]
38. Yuan, L.L.; Zhang, X.H.; Xue, F.H.; Lu, Y.H.; Zong, K.Q. Late Permian high-Mg andesite and basalt association from northern Liaoning, North China: Insights into the final closure of the Paleo-Asian ocean and the orogeny-craton boundary. *Lithos* **2016**, *258–259*, 58–76. [CrossRef]
39. Yang, D.G.; Sun, D.Y.; Gou, J.; Hou, X.G. U–Pb ages of zircons from Mesozoic intrusive rocks in the Yanbian area, Jilin Province, NE China: Transition of the Paleo-Asian oceanic regime to the circum-Pacific tectonic regime. *J. Asian Earth Sci.* **2017**, *143*, 171–190. [CrossRef]
40. Song, Z.G.; Han, Z.Z.; Gao, L.H.; Geng, H.Y.; Li, X.P.; Meng, F.X.; Han, M.; Zhong, W.J.; Li, J.J.; Du, Q.X.; et al. Permo-Triassic evolution of the southern margin of the Central Asian Orogenic Belt revisited: Insights from Late Permian igneous suite in the Daheishan Horst, NE China. *Gondwana Res.* **2018**, *56*, 23–50. [CrossRef]

41. Guan, Q.B.; Liu, Z.H.; Liu, Y.J.; Liu, J.; Wang, S.J.; Tian, Y. Geochemistry and zircon U–Pb geochronology of mafic rocks in the Kaiyuan tectonic mélange of northern Liaoning Province, NE China: Constraints on the tectonic evolution of the Paleo-Asian Ocean. *Geol. J.* **2019**, *54*, 656–678. [CrossRef]
42. Shi, Y.; Liu, Z.H.; Liu, Y.J.; Shi, S.S.; Wei, M.H.; Yang, J.J.; Gao, T. Late Paleozoic–Early Mesozoic southward subduction-closure of the Paleo-Asian Ocean: Proof from geochemistry and geochronology of Early Permian–Late Triassic felsic intrusive rocks from North Liaoning, NE China. *Lithos* **2019**, *346–347*, 105165. [CrossRef]
43. Liu, J.; Zhang, J.; Liu, Z.H.; Yin, C.Y.; Zhao, C.; Yu, X.Y.; Chen, Y.; Tian, Y.; Dong, Y. Petrogenesis of Permo-Triassic intrusive rocks in Northern Liaoning Province, NE China: Implications for the closure of the eastern Paleo-Asian Ocean. *Int. Geol. Rev.* **2020**, *62*, 754–780. [CrossRef]
44. Jing, Y.; Ge, W.C.; Dong, Y.; Yang, H.; Ji, Z.; Bi, J.H.; Zhou, H.Y.; Xing, D.H. Early–Middle Permian southward subduction of the eastern Paleo-Asian Ocean: Constraints from geochronology and geochemistry of intermediate-acidic volcanic rocks in the northern margin of the North China Craton. *Lithos* **2020**, *364–365*, 105491. [CrossRef]
45. Jing, Y.; Ji, Z.; Ge, W.C.; Dong, Y.; Yang, H.; Bi, J.H. Middle–late permian I-type granitoids from the Diaobingshan region in the northern margin of the North China Craton: Insight into southward subduction of the Paleo–Asian Ocean. *Int. Geol. Rew.* **2020**. [CrossRef]
46. Guan, Q.B.; Liu, Z.H.; Liu, Y.J.; Li, S.Z.; Wang, S.J.; Chen, Z.X.; Zhang, C. A tectonic transition from closure of the Paleo-Asian Ocean to subduction of the Paleo-Pacific Plate: Insights from early Mesozoic igneous rocks in eastern Jilin Province, NE China. *Gondwana Res.* **2020**. [CrossRef]
47. Wang, Z.J.; Xu, W.L.; Pei, F.P.; Wang, Z.W.; Li, Y. Geochronology and provenance of detrital zircons from late Palaeozoic strata of central Jilin Province, Northeast China: Implications for the tectonic evolution of the eastern Central Asian Orogenic Belt. *Int. Geol. Rev.* **2015**, *57*, 211–228. [CrossRef]
48. Liu, J.; Liu, Z.H.; Zhao, C.; Wang, C.J.; Guan, Q.B.; Dou, S.Y.; Song, S. Geochemistry and U–Pb detrital zircon ages of late Permian to Early Triassic metamorphic rocks from northern Liaoning, North China: Evidence for the timing of final closure of the Paleo-Asian Ocean. *J. Asian Earth Sci.* **2017**, *145*, 460–474. [CrossRef]
49. Zhou, Z.B.; Pei, F.P.; Wang, Z.W.; Cao, H.H.; Xu, W.L.; Wang, Z.J.; Zhang, Y. Using detrital zircons from late Permian to Triassic sedimentary rocks in the south-eastern Central Asian Orogenic Belt (NE China) to constrain the timing of the final closure of the Paleo-Asian Ocean. *J. Asian Earth Sci.* **2017**, *144*, 82–109. [CrossRef]
50. Du, Q.X.; Han, Z.Z.; Shen, X.L.; Gao, L.H.; Han, M.; Song, Z.G.; Li, J.J.; Zhong, W.J.; Yan, J.L.; Liu, H. Geochemistry and geochronology of Upper Permian-Upper Triassic volcanic rocks in eastern Jilin Province, NE China: Implications for the tectonic evolution of the Palaeo-Asian Ocean. *Int. Geol. Rev.* **2017**, *59*, 368–390. [CrossRef]
51. Du, Q.X.; Han, Z.Z.; Shen, X.L.; Han, C.; Song, Z.G.; Gao, L.H.; Han, M.; Zhong, W.J.; Yan, J.L. New evidence of detrital zircon ages for the final closure time of the Paleo-Asian Ocean in the eastern Central Asian Orogenic Belt (NE China). *Acta Geol. Sin. Engl. Ed.* **2017**, *91*, 1910–1914. [CrossRef]
52. Du, Q.X.; Han, Z.Z.; Shen, X.L.; Han, C.; Song, Z.G.; Gao, L.H.; Han, M.; Zhong, W.J. Geochronology and geochemistry of Permo-Triassic sandstones in eastern Jilin Province (NE China): Implications for final closure of the Paleo-Asian Ocean. *Geosci. Front.* **2019**, *10*, 368–390. [CrossRef]
53. Han, Z.Z.; Zhong, W.J.; Song, Z.G.; Han, C.; Han, M.; Gao, L.H.; Du, Q.X.; Li, J.J.; Yan, J.L.; Liu, H. Geochronology and geochemistry of metasedimentary rocks from the Dongnancha Formation in the Huadian area, central Jilin Province, Northeast (NE) China: Implications for the tectonic evolution of the eastern segment of the Paleo-Asian Ocean. *Geochemistry* **2019**, *79*, 94–112. [CrossRef]
54. Shen, X.L.; Du, Q.X.; Han, Z.Z.; Song, Z.G.; Han, C.; Zhong, W.J.; Ren, X. Constraints of zircon U-Pb-Hf isotopes from Late Permian-Middle Triassic flora-bearing strata in the Yanbian area (NE China) on a scissor-like closure model of the Paleo-Asian Ocean. *J. Asian Earth Sci.* **2019**, *183*, 103964. [CrossRef]
55. Dong, Y.; Ge, W.C.; Yang, H.; Bi, J.H.; Wang, Z.H.; Xu, W.L. Permian tectonic evolution of the Mudanjiang Ocean: Evidence from zircon U-Pb-Hf isotopes and geochemistry of a N-S trending granitoid belt in the Jiamusi Massif, NE China. *Gondwana Res.* **2017**, *49*, 147–163. [CrossRef]
56. Dong, Y.; Ge, W.C.; Yang, H.; Ji, Z.; He, Y.; Zhao, D.; Xu, W.L. Convergence history of the Jiamusi and Songnen-Zhangguangcai Range massifs: Insights from detrital zircon U–Pb geochronology of the Yilan Heilongjiang Complex, NE China. *Gondwana Res.* **2018**, *56*, 51–68. [CrossRef]

57. Dong, Y.; Ge, W.C.; Yang, H.; Liu, X.W.; Bi, J.H.; Ji, Z.; Xu, W.L. Geochemical and SIMS U–Pb rutile and LA–ICP–MS U–Pb zircon geochronological evidence of the tectonic evolution of the Mudanjiang Ocean from amphibolites of the Heilongjiang Complex, NE China. *Gondwana Res.* **2019**, *69*, 25–44. [CrossRef]
58. Ge, M.H.; Zhang, J.J.; Liu, K.; Ling, Y.Y.; Wang, M.; Wang, J.M. Geochemistry and geochronology of the blueschist in the Heilongjiang Complex and its implications in the late Paleozoic tectonics of eastern NE China. *Lithos* **2016**, *261*, 232–249. [CrossRef]
59. Ge, M.H.; Zhang, J.J.; Li, L.; Liu, K.; Ling, Y.Y.; Wang, J.M.; Wang, M. Geochronology and geochemistry of the Heilongjiang Complex and the granitoids from the Lesser Xing'an-Zhangguangcai Range: Implications for the late Paleozoic-Mesozoic tectonics of eastern NE China. *Tectonophysics* **2017**, *717*, 565–584. [CrossRef]
60. Ge, M.H.; Zhang, J.J.; Li, L.; Liu, K. A Triassic-Jurassic westward scissor-like subduction history of the Mudanjiang Ocean and amalgamation of the Jiamusi Block in NE China: Constraints from whole-rock geochemistry and zircon U–Pb and Lu-Hf isotopes of the Lesser Xing'an-Zhangguangcai Range granitoids. *Lithos* **2018**, *302–303*, 263–277.
61. Han, W.; Zhou, J.B.; Wilde, S.A.; Li, L. LA-ICPMS zircon U–Pb dating of the Heilongjiang Complex in the Luobei area: New constraints for the late Palaeozoic-Mesozoic tectonic evolution of Jiamusi Block, NE China. *Geol. J.* **2020**, *55*, 1644–1669. [CrossRef]
62. Long, X.Y.; Xu, W.L.; Guo, P.; Sun, C.Y.; Luan, J.P. Was Permian magmatism in the eastern Songnen and western Jiamusi massifs, NE China, related to the subduction of the Mudanjiang oceanic plate? *Geol. J.* **2020**, *55*, 1781–1807. [CrossRef]
63. Zhao, D.; Ge, W.C.; Yang, H.; Dong, Y.; Bi, J.H.; He, Y. Petrology, geochemistry, and zircon U–Pb–Hf isotopes of Late Triassic enclaves and host granitoids at the southeastern margin of the Songnen–Zhangguangcai Range Massif, Northeast China: Evidence for magma mixing during subduction of the Mudanjiang oceanic plate. *Lithos* **2019**, *312–313*, 358–374.
64. Zhou, J.B.; Wilde, S.A.; Zhao, G.C.; Zhang, X.Z.; Wang, H.; Zeng, W.S. Was the easternmost segment of the Central Asian Orogenic Belt derived from Gondwana or Siberia: An intriguing dilemma? *J. Geodyn.* **2010**, *50*, 300–317. [CrossRef]
65. Zhu, C.Y.; Zhao, G.C.; Sun, M.; Liu, Q.; Han, Y.G.; Hou, W.; Zhang, X.R.; Eizenhofer, P.R. Geochronology and geochemistry of the Yilan blueschists in the Heilongjiang complex, northeastern China and tectonic implications. *Lithos* **2015**, *216*, 241–253. [CrossRef]
66. Zhu, C.Y.; Zhao, G.C.; Sun, M.; Eizenhofer, P.R.; Liu, Q.; Zhang, X.R. Geochronology and geochemistry of the Yilan greenschists and amphibolites in the Heilongjiang complex, northeastern China and tectonic implications. *Gondwana Res.* **2017**, *43*, 213–228. [CrossRef]
67. Zhu, C.Y.; Zhao, G.C.; Sun, M.; Han, Y.G.; Liu, Q.; Eizenhofer, P.R.; Zhang, X.R.; Hou, W.Z. Detrital zircon U–Pb and Hf isotopic data for meta-sedimentary rocks from the Heilongjiang Complex, northeastern China and tectonic implications. *Lithos* **2017**, *282–283*, 23–32. [CrossRef]
68. Zhu, C.Y.; Zhao, G.C.; Ji, J.Q.; Han, Y.G.; Liu, Q.; Eizenhofer, P.R.; Zhang, X.R.; Hou, W.Z. Subduction between the Jiamusi and Songliao blocks: Geological, geochronological and geochemical constraints from the Heilongjiang Complex. *Lithos* **2017**, *282–283*, 128–144. [CrossRef]
69. Wang, B.; Zhou, J.B.; Wilde, S.A.; Zhang, X.Z.; Ren, S.M. The timing of final closure along the Changchun–Yanji suture zone: Constraints from detrital zircon U–Pb dating of the Triassic Dajianggang Formation, NE China. *Lithos* **2016**, *261*, 216–231. [CrossRef]
70. Zhou, J.B.; Wilde, S.A. The crustal accretion history and tectonic evolution of the NE China segment of the Central Asian Orogenic Belt. *Gondwana Res.* **2013**, *23*, 1365–1377. [CrossRef]
71. Zhou, J.B.; Cao, J.L.; Wilde, S.A.; Zhao, G.C.; Zhang, J.J.; Wang, B. Paleo-Pacific subduction-accretion: Evidence from geochemical and U–Pb zircon dating of the Nadanhada accretionary complex, NE China. *Tectonics* **2014**, *33*, 2444–2466. [CrossRef]
72. Zhou, J.B.; Li, L. The Mesozoic accretionary complex in Northeast China: Evidence for the accretion history of Paleo-Pacific subduction. *J. Asian Earth Sci.* **2017**, *145*, 91–100. [CrossRef]
73. Pei, F.P.; Zhang, Y.; Wang, Z.W.; Cao, H.H.; Xu, W.L.; Wang, F.; Yang, C. Early-Middle Paleozoic subduction–collision history of the south-eastern Central Asian Orogenic Belt: Evidence from igneous and metasedimentary rocks of central Jilin Province, NE China. *Lithos* **2016**, *261*, 164–180. [CrossRef]
74. Wu, F.Y.; Sun, D.Y.; Ge, W.C.; Zhang, Y.B.; Grant, M.L.; Wilde, S.A.; Jahn, B.M. Geochronology of the Phanerozoic granitoids in northeastern China. *J. Asian Earth Sci.* **2011**, *41*, 1–30. [CrossRef]

75. Wang, Z.W.; Pei, F.P.; Xu, W.L.; Cao, H.H.; Wang, Z.J. Geochronology and geochemistry of Late Devonian and early Carboniferous igneous rocks of central Jilin Province, NE China: Implications for the tectonic evolution of the eastern Central Asian Orogenic Belt. *J. Asian Earth Sci.* **2015**, *97*, 260–278. [CrossRef]
76. Zhang, H.H.; Wang, F.; Xu, W.L.; Cao, H.H.; Pei, F.P. Petrogenesis of Early–Middle Jurassic intrusive rocks in northern Liaoning and central Jilin provinces, northeast China: Implications for the extent of spatial–temporal overprinting of the Mongol–Okhotsk and Paleo-Pacific tectonic regimes. *Lithos* **2016**, *256–257*, 132–147. [CrossRef]
77. Wang, D.F.; Chen, C.Y.; Yang, S.; Yang, X.Z.; Zhang, J.F. The foundation of Early Paleozoic Qinghezhen Group in Northern Liaoning and its important geological significance. *Bull. Shenyang Inst. Geol. Miner. Res. Chin. Acad. Geol. Sci.* **1988**, *52*, 171–177. (In Chinese)
78. Huan, Y.Q.; Pei, S.J.; Chen, S.L.; Hong, Z.M.; Zhao, G.H. Ophiolitic mélange in the Kaiyuan group. *Reg. Geol. Chin.* **1999**, *18*, 4–13. (In Chinese)
79. Chen, Y.J.; Peng, Y.J.; Liu, Y.W.; Sun, G.; Matthew, G. Progress in the study of chronostratigraphy of the "Qinghezhen Group". *Geol. Rev.* **2006**, *52*, 171–177. (In Chinese)
80. Liu, J.; Liu, Z.H.; Zhao, C.; Wang, C.J.; Peng, Y.B.; Zhang, H. Petrogenesis and zircon LA-ICP-MS U–Pb dating of newly discovered Mesoarchean gneisses on the northern margin of the North China Craton. *Int. Geol. Rev.* **2017**, *59*, 1575–1589. [CrossRef]
81. Chi, Y.Y.; Su, Y.Z.; Nan, R.S. Division and age of Hulan Group in Hulanzhen area of central Jilin. *Acta Geosci. Sinica* **1997**, *18*, 205–214. (In Chinese)
82. Xi, A.H.; Ren, H.M.; Zhang, B.F.; Wang, Y.X.; Shi, S.B.; Zhi, X.J. Isotopic chronology of the Hulan Group and its geological significance in the Central Jilin Province. *J. Jilin Uni. Earth Sci.* **2003**, *33*, 15–18. (In Chinese)
83. Wang, Y.Q.; Su, Y.Z.; Liu, E.Y. *Multiple Correlation Research on the Strata of China–the Regional Strata of the Northeast China*; China University of Geosciences Press: Wuhan, China, 1997; pp. 1–175. (In Chinese)
84. Nan, R.S.; Guo, S.Z. *Paleozoic Biostratigraphy and Lithofacies-Paleogeography of Eastern Jilin and Heilongjiang Provinces, China*; Geological Publishing House: Beijing, China, 1992; pp. 1–146. (In Chinese)
85. Whitney, D.L.; Evans, B.W. Abbreviations for names of rock-forming minerals. *Am. Mineral.* **2010**, *95*, 185–187. [CrossRef]
86. Yuan, H.L.; Gao, S.; Liu, X.M.; Li, H.M.; Günther, D.; Wu, F.Z. Accurate U–Pb age and trace element determinations of zircon by laser ablation inductively coupled plasma mass spectrometry. *Geostand. Geoanal. Res.* **2004**, *28*, 353–370. [CrossRef]
87. Van Achterbergh, E.; Ryan, C.G.; Jackson, S.E.; Griffin, W.L. Data reduction software for LA–ICP–MS. In *Laser–Ablation–ICP–MS Spectrometry in the Earth Sciences: Principles and Applications*; Sylvester, P.J., Ed.; Mineralogical Association of Canada, MAC Short Course Series: Ottawa, ON, Canada, 2001; Volume 29, pp. 239–243.
88. Ludwig, K.R. User's manual for Isoplot 3.00: A geochronological toolkit for Microsoft Excel. *Berkeley Geochronol. Cent.* **2003**, *4*, 1–70.
89. Rudnick, R.L.; Gao, S.; Ling, W.L.; Liu, Y.S.; McDonough, W.F. Petrology and geochemistry of spinel peridotite xenoliths from Hannuoba and Qixia, North China craton. *Lithos* **2004**, *7*, 609–637. [CrossRef]
90. Li, X.H. Geochemistry of the Longsheng Ophiolite from the southern margin of Yangtze Craton, SE China. *Geochem. J.* **1997**, *31*, 323–337. [CrossRef]
91. Xu, P.; Wu, F.Y.; Xie, L.W.; Yang, Y.H. Hf isotopic compositions of the standard zircons for U–Pb dating. *Chin. Sci. Bull.* **2004**, *49*, 1642–1648. [CrossRef]
92. Chu, N.C.; Taylor, R.N.; Chavagnac, V.; Nesbitt, R.W.; Boella, R.M.; Milton, J.A.; German, C.R.; Bayon, G.; Burton, K. Hf isotope ratio analysis using multi–collector inductively coupled plasma mass spectrometry: An evaluation of isobaric interference corrections. *J. Anal. At. Spectrom.* **2002**, *17*, 1567–1574. [CrossRef]
93. Albarède, F.; Scherer, E.E.; Blichert–Toft, J.; Rosing, M.; Simionovici, A.; Bizzarro, M. γ–ray irradiation in the early Solar System and the conundrum of the ^{176}Lu decay constant. *Geochim. Cosmochim. Acta* **2006**, *70*, 1261–1270. [CrossRef]
94. Bouvier, A.; Vervoort, J.D.; Patchett, P.J. The Lu–Hf and Sm–Nd isotopic composition of CHUR: Constrains from unequilibrated chondrites and implications for the bulk composition of terrestrial planets. *Earth Planet. Sci. Lett.* **2008**, *273*, 48–57. [CrossRef]

95. Griffin, W.L.; Pearson, N.J.; Belousova, E.; Jackson, S.E.; van Achterbergh, E.; O'Reilly, S.Y.; Shee, S.R. The Hf isotope composition of cratonic mantle: LAM–MC–ICPMS analysis of zircon megacrysts in kimberlites. *Geochim. Cosmochim. Acta* **2000**, *64*, 133–147. [CrossRef]
96. Zhou, S.T. *Geology of Banded Iron Formations in the Anshan–Benxi Area*; Geological Publishing House: Beijing, China, 1994; pp. 1–278. (In Chinese)
97. Winchester, J.A.; Max, M.D.; Long, C.B. Trace element correlation in the reworked Proterozoic Dalradian metavolcanic suites of the western Ox Mountains and NW Mayo inliers, Ireland. In *Geochemistry and Mineralization of Proterozoic Volcanic Suites*; Pharaoh, T., Beckinsale, R.D., Rickard, D., Eds.; Geological Society of London Special Publication: London, UK, 1987; Volume 33, pp. 489–502.
98. Shaw, D.M. The Origin of the Apsley Gneiss, Ontario. *Can. J. Earth Sci.* **1972**, *9*, 18–35. [CrossRef]
99. Winchester, J.A.; Floyd, P.A. Geochemical discrimination of different magma series and their differentiation products using immobile elements. *Chem. Geol.* **1977**, *20*, 325–343. [CrossRef]
100. Sun, S.S.; McDonough, W.F. Chemical and isotopic systematics of oceanic basalts: Implications for mantle composition and processes. In *Magmatism in Ocean Basins*; Saunders, A.D., Norry, M.J., Eds.; Geological Society of London Special Publication: London, UK, 1989; Volume 42, pp. 313–345.
101. Corfu, F.; Hanchar, J.M.; Hoskin, P.W.O.; Kinny, P. Atlas of zircon textures. *Rev. Mineral. Geochem.* **2003**, *53*, 469–500. [CrossRef]
102. Bingen, B.; Austrheim, H.; Whitehouse, M.J.; Davis, W.J. Trace element signature and U–Pb geochronology of eclogite-facies zircon, Bergen Arcs, Caledonides of Western Norway. *Contrib. Mineral. Petrol.* **2004**, *147*, 671–683. [CrossRef]
103. Cao, Y.T.; Liu, L.; Chen, D.L.; Wang, C.; Yang, W.Q.; Kang, L.; Zhu, X.H. Partial melting during exhumation of Paleozoic retrograde eclogite in North Qaidam, western China. *J. Asian Earth Sci.* **2017**, *148*, 223–240. [CrossRef]
104. Song, Z.J.; Liu, H.M.; Meng, F.X.; Yuan, X.Y.; Feng, Q.; Zhou, D.W.; Romaní, J.R.V.; Yan, H.B. Zircon U–Pb Ages and Hf Isotopes of Neoproterozoic Meta-Igneous Rocks in the Liansandao Area, Northern Sulu Orogen, Eastern China, and the Tectonic Implications. *J. Earth Sci.* **2019**, *30*, 1230–1242. [CrossRef]
105. Song, Z.J.; Meng, F.X.; Li, H.F.; Yuan, X.Y.; Li, X.P.; Xu, Q.L. Dating of zircon LA-MC-ICP-MS U–Pb in metabasalt of zhaertai group, Inner Mongolia, China. *Indian J. Geo-Mar. Sci.* **2017**, *46*, 1950–1958.
106. Mezger, K.; Krogstad, E.J. Interpretation of discordant U–Pb zircon ages: An evaluation. *J. Metamorph. Geol.* **1997**, *15*, 127–140. [CrossRef]
107. Cao, Y.T.; Liu, L.; Wang, C.; Kang, L.; Li, D.; Yang, W.Q.; Zhu, X.H. Timing and nature of the partial melting processes during the exhumation of the garnet–bearing biotite gneiss in the southern Altyn Tagh HP/UHP belt, Western China. *J. Asian Earth Sci.* **2019**, *170*, 274–293. [CrossRef]
108. Wang, S.J.; Li, X.P.; Schertl, H.P.; Feng, Q.D. Petrogenesis of early cretaceous andesite dykes in the Sulu orogenic belt, eastern China. *Miner. Petrol.* **2019**, *113*, 77–97. [CrossRef]
109. Hoskin, P.W.O. Trace-element composition of hydrothermal zircon and the alteration of Hadean zircon from the Jack Hills, Australia. *Geochim. Cosmochim. Acta* **2005**, *69*, 637–648. [CrossRef]
110. Zhao, G.C.; Sun, M.; Wilde, S.A.; Li, S.Z. Late Archean to Paleoproterozoic evolution of the North China Craton: Key issues revisited. *Precambrian Res.* **2005**, *136*, 177–202. [CrossRef]
111. Cao, J.L.; Zhou, J.B.; Li, L. The tectonic evolution of the Changchun-Yanji suture zone: Constraints of zircon U–Pb ages of the Yantongshan accretionary complex (NE China). *J. Asian Earth Sci.* **2020**, *194*, 104110. [CrossRef]
112. Polat, A.; Hofmann, A.W.; Rosing, M.T. Boninite-like volcanic rocks in the 3.7–3.8 Ga Isua greenstone belt, West Greenland: Geochemical evidence for intra-oceanic subduction zone processes in the early Earth. *Chem. Geol.* **2002**, *184*, 231–254. [CrossRef]
113. Condie, K.C.; Viljoen, M.J.; Kable, E.J.D. Effects of alteration on element distributions in archean tholeiites from the Barberton greenstone belt, South Africa. *Contrib. Miner. Petrol.* **1977**, *64*, 75–89. [CrossRef]
114. Dostal, J.; Strong, D.F.; Jamieson, R.A. Trace element mobility in the mylonite zone within the ophiolite aureole, St. Anthony Complex, Newfoundland. *Earth Planet. Sci. Lett.* **1980**, *49*, 188–192. [CrossRef]
115. Liu, J.Q.; Yin, P.; Chen, X.Y.; Cao, K. Distribution, Enrichment and Transport of Trace Metals in Sediments from the Dagu River Estuary in the Jiaozhou Bay, Qingdao, China. *Minerals* **2019**, *9*, 545. [CrossRef]
116. Song, Z.J.; Li, J.P.; Meng, F.X.; Tang, W.J.; Yuan, X.Y. Seasonal Distribution of Suspended Particulate Matter off China's Subei Coast. *Pol. J. Environ. Stud.* **2018**, *27*, 845–852. [CrossRef]

117. Ludden, J.; Gélinas, L.; Trudel, P. Archean metavolcanics from the Rouyn-Noranda district, Abitibi Greenstone Belt, Quebec. 2. Mobility of trace elements and petrogenetic constraints. *Can. J. Earth Sci.* **1982**, *19*, 2276–2287. [CrossRef]
118. Rundnick, R.L.; Gao, S. Composition of the continental crust. In *Treatise on Geochemistry*; Holland, H.D., Turekian, K., Eds.; Elsevier: Amsterdam, The Netherlands, 2004; Volume 3, pp. 1–64.
119. Salters, V.J.M.; Stracke, A. Composition of the depleted mantle. *Geochem. Geophys. Geosyst.* **2004**, *15*, Q05004. [CrossRef]
120. Taylor, S.R.; McLennan, S. The geochemical evolution of the continental crust. *Rev. Geophys.* **1995**, *33*, 241–265. [CrossRef]
121. Plank, T. Constraints from thorium/lanthanum on sediment recycling at subduction zones and the evolution of the continents. *J. Petrol.* **2005**, *46*, 921–944. [CrossRef]
122. Dasgupta, R.; Hirschmann, M.M.; Smith, N.D. Partial melting experiments of peridotite + CO_2 at 3 GPa and genesis of alkalic ocean island basalts. *J. Petrol.* **2007**, *48*, 2093–2124. [CrossRef]
123. Pilet, S.; Baker, M.B.; Stolper, E.M. Metasomatized lithosphere and the origin of alkaline lavas. *Science* **2008**, *320*, 916–919. [CrossRef]
124. Sobolev, A.V.; Hofmann, A.W.; Sobolev, S.V.; Nikogosian, I.K. An olivine-free mantle source of Hawaiian shield basalts. *Nature* **2005**, *434*, 590–597. [CrossRef]
125. Eggler, D.H. The effect of CO_2 upon partial melting of peridotite in the system Na_2O-CaO-Al_2O_3-MgO-SiO_2-CO_2 to 35 kb, with an analysis of melting in a peridotite-H_2O-CO_2 system. *Am. J. Sci.* **1978**, *278*, 305–343. [CrossRef]
126. Herzberg, C. Petrology and thermal structure of the Hawaiian plume from Mauna Kea volcano. *Nature* **2006**, *444*, 605–609. [CrossRef]
127. Hirschmann, M.M.; Kogiso, T.; Baker, M.B.; Stolper, E.M. Alkalic magmas generated by partial melting of garnet pyroxenite. *Geology* **2003**, *31*, 481–484. [CrossRef]
128. Hirose, K.; Kushiro, I. Partial melting of dry peridotites at high pressures: Determination of compositions of melts segregated from peridotite using aggregates of diamond. *Earth Planet. Sci. Lett.* **1993**, *114*, 477–489. [CrossRef]
129. Hirose, K. Partial melt compositions of carbonated peridotite at 3 GPa and role of CO_2 in alkali-basalt magma generation. *Geophys. Res. Lett.* **1997**, *24*, 2837–2840. [CrossRef]
130. Walter, M.J. Melting of garnet peridotite and the origin of komatiite and depleted lithosphere. *J. Petrol.* **1998**, *39*, 29–60. [CrossRef]
131. Kogiso, T.; Hirschmann, M.M.; Frost, D.J. High-pressure partial melting of garnet pyroxenite: Possible mafic lithologies in the source of ocean island basalts. *Earth Planet. Sci. Lett.* **2003**, *216*, 603–617. [CrossRef]
132. Dasgupta, R.; Hirschmann, M.M.; Stalker, K. Immiscible transition from carbonaterich to silicate-richmelts in the 3 GPa melting interval of eclogite + CO_2 and genesis of silica-undersaturated ocean island lavas. *J. Petrol.* **2006**, *47*, 647–671. [CrossRef]
133. Hofmann, A.W. Chemical differentiation of the earth: The relationship between mantle, continental crust, and oceanic crust. *Earth Planet. Sci. Lett.* **1988**, *90*, 297–314. [CrossRef]
134. Tischendorf, G.; Paelchen, W. On the classification of granitoids. *Z. Geol. Wiss.* **1985**, *13*, 615–627.
135. Romaní, J.R.V.; Song, Z.J.; Liu, H.M.; Sun, Y.F.; Li, H.N. Orogenic Movements during the Paleozoic Period: Development of the Granitoid Formations in the Northwestern Region of Spain's Iberian Peninsula. *J. Earth Sci.* **2020**, *31*, 611–620. [CrossRef]
136. Chappell, B.W.; White, A. I- and S-type granites in the Lachlan Fold Belt. *Earth Environ. Sci. Trans. R. Soc. Edinb.* **1992**, *83*, 1–26.
137. Meng, Y.K.; Xiong, F.H.; Xu, Z.Q.; Ma, X.X. Petrogenesis of Late Cretaceous mafic enclaves and their host granites in the Nyemo region of southern Tibet: Implications for the tectonic-magmatic evolution of the Central Gangdese Belt. *J. Asian Earth Sci.* **2019**, *176*, 27–41. [CrossRef]
138. Wang, S.J.; Schertl, H.P.; Pang, Y.M. Geochemistry, geochronology and Sr–Nd–Hf isotopes of two types of Early Cretaceous granite porphyry dykes in the Sulu orogenic belt, eastern China. *Can. J. Earth Sci.* **2020**, *57*, 249–266. [CrossRef]
139. Du, L.; Zhang, Y.Y.; Huang, Z.Y.; Li, X.P.; Yuan, C.; Wu, B.; Long, X.P. Devonian to carboniferous tectonic evolution of the Kangguer Ocean in the Eastern Tianshan, NW China: Insights from three episodes of granitoids. *Lithos* **2019**, *350–351*, 105243. [CrossRef]

140. Du, L.; Yuan, C.; Li, X.P.; Zhang, Y.Y.; Huang, Z.Y.; Long, X.P. Petrogenesis and Geodynamic Implications of the Carboniferous Granitoids in the Dananhu Belt, Eastern Tianshan Orogenic Belt. *J. Earth Sci.* **2019**, *30*, 1243–1252. [CrossRef]
141. Pang, Y.M.; Guo, X.W.; Zhang, X.H.; Zhu, X.Q.; Hou, F.H.; Wen, Z.H.; Han, Z.Z. Late Mesozoic and Cenozoic tectono-thermal history and geodynamic implications of the Great Xing'an Range, NE China. *J. Asian Earth Sci.* **2020**, *189*, 104155. [CrossRef]
142. Yu, Q.; Ge, W.C.; Yang, H.; Zhao, G.C.; Zhang, Y.L.; Su, L. Petrogenesis of late Paleozoic volcanic rocks from the Daheshen Formation in central Jilin Province, NE China, and its tectonic implications: Constrains from geochronology, geochemistry and Sr-Nd-Hf isotopes. *Lithos* **2014**, *192–195*, 116–131. [CrossRef]
143. Whalen, J.B.; Currie, K.L.; Chappell, B.W. A-type granites: Geochemical characteristics, discrimination and petrogenesis. *Contrib. Mineral. Petrol.* **1987**, *95*, 407–419. [CrossRef]
144. Martin, H. Effect of steeper Archaean geothermal gradient on geochemistry of subduction-zone magmas. *Geology* **1986**, *14*, 753–756. [CrossRef]
145. Pearce, J.A.; Norry, M.J. Petrogenetic implications of Ti, Zr, Y and Nb variations in volcanic rocks. *Contrib. Mineral. Petrol.* **1979**, *69*, 33–47. [CrossRef]
146. Xiong, F.H.; Meng, Y.K.; Yang, J.S.; Liu, Z.; Xu, X.Z.; Eslami, A.; Zhang, R. Geochronology and petrogenesis of the mafic dykes from the Purang ophiolite: Implications for evolution of the western Yarlung-Tsangpo suture zone, southwestern Tibet. *Geosci. Front.* **2020**, *11*, 227–292. [CrossRef]
147. Turner, S.; Arnaud, N.; Liu, J.; Rogers, N.; Hawkesworth, C.; Harris, N.; Kelley, S.; Van Calsteren, P.; Deng, W. Post-collision, shoshonitic volcanism on the Tibetan Plateau: Implications for convective thinning of the lithosphere and the source of ocean island basalts. *J. Petrol.* **1996**, *37*, 45–71. [CrossRef]
148. Yan, J.; Chen, J.F.; Xu, X.S. Geochemistry of Cretaceous mafic rocks from the Lower Yangtze region, eastern China: Characteristics and evolution of the lithospheric mantle. *J. Asian Earth Sci.* **2008**, *33*, 177–193. [CrossRef]
149. Rogers, G.; Hawkesworth, C.J. A geochemical traverse across the North Chilean Andes: Evidence for crust generation from the mantle wedge. *Earth Planet. Sci. Lett.* **1989**, *91*, 271–285. [CrossRef]
150. Sajona, F.G.; Maury, R.C.; Bellon, H.; Cotton, J.; Defant, M. High field strength elements of Pliocene–Pleistocene island–arc basalts Zamboanga Peninsula, Western Mindanao (Philippines). *J. Petrol.* **1996**, *37*, 693–726. [CrossRef]
151. Kelemen, P.B.; Hanghøj, K.; Greene, A.R. One view of the geochemistry of subduction-related magmatic arcs, with an emphasis on primitive andesite and lower crust. *Treatise Geochem.* **2007**, *138*, 1–70.
152. Wu, F.Y.; Wilde, S.A.; Sun, D.Y.; Zhang, G.L. Geochronology and petrogenesis of post-orogenic Cu, Ni-bearing mafic–ultramafic intrusions in Jilin, NE China. *J. Asian Earth Sci.* **2004**, *23*, 781–797. [CrossRef]
153. Xie, H.Q.; Zhang, F.Q.; Miao, L.C.; Li, T.S.; Liu, D.Y. Characteristics of the Piaohechuan mafic-ultramafic complex, central Jilin, Northeast China: Constrains on the nature and evolution of the northeastern North China marginal tectonic belt. *Geol. Bull. China* **2007**, *26*, 810–822. (In Chinese)
154. Wang, F.; Xu, W.L.; Ge, W.C.; Yang, H.; Pei, F.P.; Wu, W. The offset distance of the Dunhua-Mishan Fault: Constraints from Paleozoic-Mesozoic magmatism within the Songnen-Zhangguangcai Range, Jiamusi, and Khanka massifs. *Acta Petrol. Sin.* **2016**, *32*, 1129–1140. (In Chinese)